



Review on mechanical and functional properties of refractory high-entropy alloy films by magnetron sputtering

Mohamed El Garah^{1,2} · Driss Soubane^{3,4} · Frederic Sanchette^{1,2}

Received: 25 September 2023 / Accepted: 5 December 2023 / Published online: 30 December 2023
© The Author(s) 2023

Abstract

Refractory high-entropy films (RHEFs), as multi-component materials, have garnered significant attention due to their potential use in high-temperature applications. RHEFs are endowed with unique microstructural and functional properties due to the use of refractory elements. In this review, we examine the recent state of research on RHEFs deposited by the magnetron sputtering technique. The microstructure of RHEFs has been analyzed/explored and the mechanical properties as well as the main hardening mechanisms of these films are discussed. Furthermore, functional properties such as resistance to corrosion and wear, electrical and irradiation performances, and high-temperature oxidation were evaluated. RHEFs can meet market demand in the field of engineering materials. However, many challenges, such as low ductility at room temperature, remain to be overcome. This review provides an overview of the strengths and weaknesses of RHEFs produced using magnetron sputtering.

Keywords Refractory high-entropy films · Magnetron sputtering · Computational · Modeling · Corrosion · Electrical · Irradiation · Oxidation

1 Introduction

High-entropy alloys (HEAs) are a relatively novel class of metallic materials that have gained significant interest in materials science and engineering. They were independently introduced, in 2004, by two separate research

groups, namely J.-W. Yeh and B. Cantor [1, 2]. Traditionally, alloys consist of one or two principal elements with a small concentration to enhance specific properties. In fact, the addition of a small amount of an alloying element to a metal can result in the improvement of its properties. For example, the addition of carbon to iron leads to the production of steel with improved mechanical strength. High corrosion resistance of stainless steel can also be obtained by adding chromium. A multielement system can be obtained by mixing various elements. In the case where the elements have different concentrations, the study of the multi-element will be difficult since intermetallic compounds can be formed. In contrast, HEAs are composed of multiple principal elements in roughly equimolar proportions, typically five or more, with each element contributing significantly to the composition of the material. They are seen as an alternative solution to improve the physicochemical properties of the materials. Since their invention, various names have been reported such as compositionally complex alloys [3], multi-principal element alloys [4], multi-component alloys [2], and complex concentrated alloys [5].

High-entropy films (HEFs), which are cost-effective, have also been investigated [6–13] and have revealed interesting

Mohamed El Garah and Driss Soubane have equal contribution.

✉ Mohamed El Garah
mohamed.el_garah@utt.fr

Driss Soubane
driss.soubane@inrs.ca

- ¹ LASMIS, Antenne de Nogent – 52, Pôle Technologique de Sud – Champagne, 52800 Nogent, France
- ² Nogent International Center for CVD Coating Innovation (NICCI), LRC CEA-LASMIS, Pôle Technologique de Sud – Champagne, 52800 Nogent, France
- ³ Laboratoire des Matériaux pour l’Energie et l’Environnement M2ELab., Faculté Polydisciplinaire de Safi, Université Cadi Ayyad, 46000 Safi, Morocco
- ⁴ Advanced Laser Light Source (ALLS), Centre Energie, Matériaux et Télécommunications, Institut National de la Recherche Scientifique INRS-EMT, Varennes, Québec J3X 1S2, Canada

physical and chemical properties. The characteristic key of HEAs and HEFs are presented below:

- High configurational entropy: The random arrangement of multiple elements in equimolar proportions constructs a highly disordered crystal structure, resulting in enhanced mechanical and thermal properties.
- Good mechanical properties [14, 15]: HEAs are often known to display outstanding mechanical features such as high strength, hardness, and ductility, revealing their attractive uses in different engineering applications [16].
- Thermodynamic stability: The high-entropy composition enables stabilizing solid solutions and prevents phase transformations at elevated temperatures.

HEFs share some similarities with HEAs, but they are specifically characterized by their microscale or nanoscale thickness and interesting physical and chemical properties. HEFs have applications in areas like coatings, electronic devices, and sensors, where thin and functional materials are required. Here are the primary characteristics of HEFs.

- Conformal coating: HEFs can be deposited as thin, conformal films on various substrates, ensuring uniform coverage even on complex geometries, especially in the case of printed circuit boards.
- Tailorable properties: The combination of different elements in the high-entropy composition enables researchers to tune the film's properties for specific applications [11, 17].
- Enhanced surface properties: The nanoscale and microscale thickness of HEFs [18] results in distinctive surface properties and interactions, rendering them substantially valuable for surface engineering.

HEAs and HEFs are investigated through a combination of experimental research, materials characterization, and theoretical modeling. Scientists and researchers employ various techniques, including X-ray diffraction, scanning electron microscopy, transmission electron microscopy, and atomic force microscopy to analyze the microstructure, composition, and properties of these materials. Additionally, computational methods such as density functional theory (DFT) and molecular dynamics simulations contribute to understanding the thermodynamic stability and mechanical behavior of HEAs and HEFs. By systematically studying and comparing the properties of these materials, scientists can identify the unique features and potential applications within each material class. In general, HEAs can be classified into two main categories: 3d transition metals and refractory metals, depending on their constituent elements. Additionally, other alloys composed of 4f transition metals should also be considered. Researchers are actively striving

to develop techniques aimed at obtaining RHEFs. The challenges posed by the high melting points of the elements in manufacturing are being addressed by the advances in high entropy. These developments allow the production of films made from RHEAs that can maintain their integrity under high-temperature conditions, which holds significant value for various industries. Magnetron sputtering is one of the preferred methods to prepare these films, and it has a remarkable ability to effectively enhance pivotal features, including mechanical and tribological properties, as well as oxidation and corrosion resistance. RHEFs with good hardness and Young's modulus have been reported in the literature. Generally, RHEFs prepared using magnetron sputtering exhibit enhanced mechanical properties and hold the potential to open up opportunities for developing applications in the field of surface treatment.

Focusing on the study of RHEFs by magnetron sputtering, this review provides an overview of their microstructure, phase, and mechanical properties (hardness and Young's modulus). It explores their structure and the impact of various deposition parameters, while also examining their functional properties such as corrosion and oxidation resistance, electrical properties, irradiation behavior, and nanolattice characteristics. Additionally, insights into HEAs are provided, covering their characteristics, phase parameter selection, and theoretical investigations. Section 2 delves into the thermodynamic aspects of HEAs, while the following section focusses on the different magnetron sputtering modes used to prepare RHEFs including details on targets preparation. The last sections present a comprehensive view of both the classical and the functional properties of RHEFs, with an extensive overview of the theoretical aspects.

2 Thermodynamics of high-entropy alloys

2.1 Solid solution thermodynamics: phase formation rules

Micro-structural complexity has been introduced as an additional criterion for classifying HEAs/HEFs. The preference for the formation of single-phase solid solution over intermetallic compounds can be the result of a low Gibbs energy:

$$\Delta G_{mix} = \Delta H_{mix} - T\Delta S_{mix} \quad (1)$$

ΔG_{mix} is composed of mixing enthalpy (ΔH_{mix}), the temperature (T), and the mixing entropy (ΔS_{mix}). Effectively, it should manifest as a single-phase disordered solid solution [19].

When studying a complex system, the Gibbs energy is subsequently linked to the enthalpy of the system.

Moreover, as presented above, the system's entropy is defined according to the Boltzmann equation [20, 21]. It is worth noting to remember that the total Gibbs free energy arises from contributions of atom vibration, electron stochasticity, magnetic dipole, and configuration. Among these contributions, the configurational aspect is the most prominent, while the other three are regularly neglected [22]. From the data above, we figure out that the rules governing phase formation are determined and derived from the term: $\Delta H_{\text{mix}} - T\Delta S_{\text{mix}}$.

Furthermore, the Hume-Rothery binary-formation rules [23, 24] combined with Inoues's empirical rules for creating bulk metallic glasses [24] highlighted the compound structure. This structural characteristic, among others, contributes to the total Gibbs free energy.

2.2 High entropy definition

The definition of HEAs has gradually become more sophisticated over time. Initially, in the very beginning, the distinction of HEAs was based merely on the complexity of their composition [25] where more than five major metallic elements are concentrated in the range of 5–35 at.%. The name “HEA” was related to the configurational entropy, which can be calculated using the following formula:

$$\Delta S_{\text{conf}} = -R \sum_{i=1}^n c_i \ln c_i \quad (2)$$

where R is the molar gas constant $R = 8.3145 \text{ J mol}^{-1} \text{ K}^{-1}$ and c_i is the concentration of the i th element [5].

From a physics perspective and considering the thermodynamics aspect, greater composition complexity within a solid solution corresponds to higher configurational entropy [26]. Moreover, inevitably, the minimum entropy threshold for a material to be classified as a high-entropy alloy (HEA) is $1.5 R$ [27].

According to the Boltzmann equation, materials like steel and Ti/Al alloys are classified as low-entropy alloys with $S \lesssim R$, while Ni/Co-based superalloys and bulk metallic glasses are categorized as medium-entropy alloys, where S falls within the range of $1R$ to $1.5 R$ [26]. This classification is illustrated in Fig. 1.

The significant interest in the novel concept of HEAs arises from their distinctive properties. Four fundamental effects have been identified as specific criteria for characterizing HEAs: the high-entropy effect, lattice deformation effect, sluggish diffusion, and cocktail effect [28, 29]. It is noteworthy that these effects were initially reported in the early publications on HEAs. A brief overview of these effects is given below.

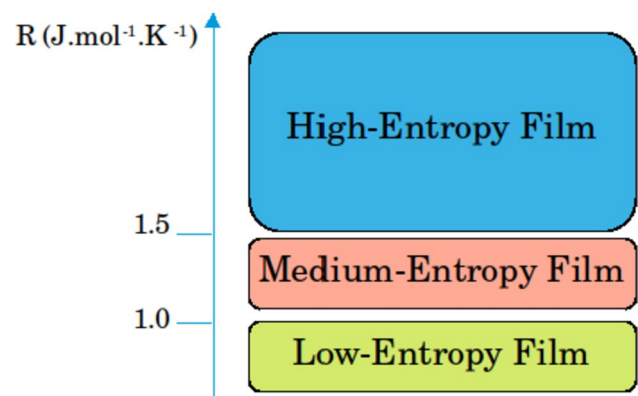


Fig. 1 High entropy alloys classification based on R value

a. High-entropy effect

In the case of HEAs, the configurational entropy is high and assumed to be the dominant term in free enthalpy. This inclination leads to a decrease in the system's Gibbs energy, favoring the prevalence of solid solutions over the intermetallic compounds provided that the enthalpy of formation is not excessively high in absolute. These special alloys are supported by an elevated entropy, significantly surpassing that of pure elements.

b. Lattice distortion

Significant distortion of the crystal lattice might arise from variations in atomic size among constituent elements. This difference results in notable implications for the physical and mechanical characteristics of HEAs [30, 31]. For instance, the elevated yield strength in these alloys could be attributed to the presence of closely spaced obstacles that hinder dislocation movement, rendering plastic deformation more challenging.

The formation of HEFs involves combining different elements with varying atomic sizes, bonding energies, and crystal structures, resulting in significant strain and stress.

c. Slow diffusion

Slow diffusion within HEAs has several significant effects. It hinders grain growth, minimizes particle alterations, and enables the attainment of a supersaturated state, enhancing overall resistance and leading to a superior recrystallization temperature [32, 33]. Diffusion in HEAs is presumed to be slower than in conventional alloys, possibly due to fluctuations in chemical bonding within the crystal lattice. Tsai et al. confirmed this in the case of CoCrFeMnNi HEA. They demonstrated that diffusion coefficients are lower for the quinary alloy compared to the pure CFC constituent elements, such as

those found in the CrFeNiSi alloy. This lower diffusion rate limits phase transformations.

d. Cocktail effect

The concept was first introduced in the work of Ranganathan [34]. Intuitively, the unique nature of HEAs allows for the combined influence of each element comprising the alloy, along with the lattice mismatch that induces distortion across the entire lattice. This effect enables the alteration of alloy properties through changes in composition. However, it is worth noting that the cocktail effect is not precisely defined, and the practice of modifying alloy composition to achieve desired properties is not exclusive to HEAs.

2.3 Phase selection rules

To predict the formation of a single-phase solid solution, semi-empirical parameters derived from thermodynamics, or inspired by rules by Hume-Rothery, have been proposed. The occurrence of phase transformation hinges then on Gibbs free energy, as discussed earlier. In comparison to intermetallic compounds, a solid solution exhibits a larger configurational entropy. The term $T\Delta S_{\text{mix}}$ indicates that solid solutions can become more stable at higher temperatures. Additionally, enthalpy is another critical factor that warrants consideration. In certain cases of HEAs, a negative enthalpy can lead to the

formation of intermetallic compounds. To address this, a new term Ω has been introduced, with its formula given below:

$$\Omega = \frac{T\Delta S_{\text{mix}}}{|\Delta H_{\text{mix}}|} \quad (3)$$

where T represents the temperature. If $\Omega > 1$, the term $T\Delta S_{\text{mix}}$ will exceed ΔH_{mix} potentially promoting the formation of a solid solution.

Conversely, the atomic size mismatch δ can significantly influence solid solution stability. According to Hume-Rothery rules [35], the difference between the elements constituting the alloys should not exceed 15%. A graphical representation of the parameters ΔH_{mix} and δ , shown in Fig. 2, allows us to define the solid solution domain.

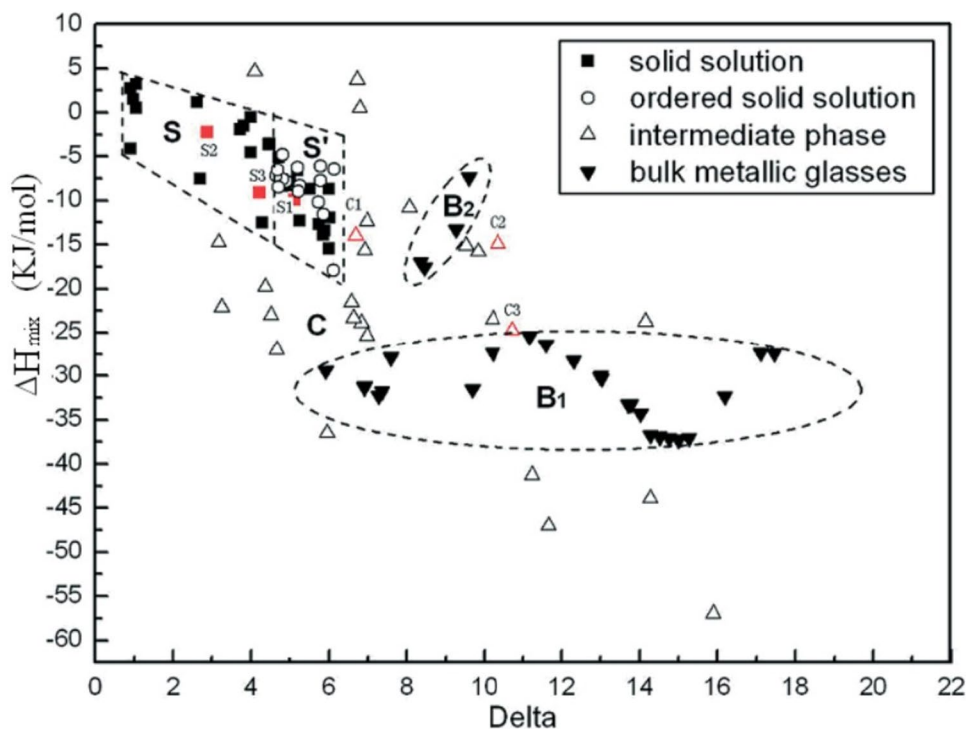
The atomic size mismatch is defined by:

$$\delta = \sqrt{\sum_{i=1}^n c_i (1 - r_i / \sum_{j=1}^n c_j r_j)^2} \quad (4)$$

where δ is the atomic size mismatch, n is the number of elements, c_i is the concentration of the i th element, r_i is the atomic radius of the i th element, and r_j is the atomic radius of the j th element.

In addition to these parameters, with the help of phase prediction in the case of HEAs, valence electron concentration (VEC) seems to be the most relevant one for predicting the structure. VEC is defined by:

Fig. 2 The selection rules for HEAs and BMGs take into account factors such as the mixing enthalpy and the atomic size difference, denoted as Delta (δ). Figure reproduced and adapted with permission from reference [22]



$$\text{VEC} = \sum_i^n c_i(\text{VEC})_i \quad (5)$$

$(\text{VEC})_i$ is the valence electron of the i th element.

An alloy with $\text{VEC} < 6.7$ is expected to exhibit a bcc structure, while an alloy with $\text{VEC} > 8$ is more likely to adopt an fcc structure. If the VEC falls between these two values, the alloy is typically dual-phased (bcc + fcc).

All these phase selection parameters have been proposed to assist in designing new compositions capable of forming solid solutions in the case of HEAs. As outlined above, they are precisely identified to predict the solid solution based on Ω and δ . VEC helps determine the crystal structure of the alloy. Discussions on these thermodynamic criteria have been reported with examples [5, 29, 36]. However, they remain empirical and do not always ensure reliable microstructure prediction. While they have proven more or less useful for HEAs, further research is necessary in the case of HEFs, including RHEFs, to gain a better understanding of their applicability, peculiarly in the context of ceramics.

One approach that could help to correlate these criteria with the characteristic of HEFs is the combinatory strategy using the magnetron sputtering technique. It is known that fabricating films by magnetron sputtering corresponds to a high cooling rate (10^9 K/s) compared to other deposition techniques. This capability can be exploited to produce a large quantity, especially in the case of HEFs, enabling the construction of a library. The resulting data can be analyzed providing the possibility to correlate them with existing rules or suggest new ones.

3 Magnetron sputtering process

Various techniques have been used to deposit RHEFs such as laser cladding [37], vacuum arc melting, and vacuum sputtering [38]. Nevertheless, since the review focuses on the recent works reported on RHEFs that are obtained by magnetron sputtering, its working principle will be presented in the following paragraphs.

The magnetron sputtering technique is highly regarded in industrial material coating. Using the process in a reactive environment is very appealing for the cost-effective preparation of materials, including nitrides, carbides, and oxides. Various materials have been successfully coated using the basic sputtering process. Energetic ions, generated in plasma, bombard a cathode leading to the deposition of the target elements [39–41]. The process can be done in a closed chamber under low pressure (Fig. 3). The sputtering is a glow discharge that occurs when voltage is applied to the cathode. The target then is held at a high negative potential and secondary electrons are accelerated from the

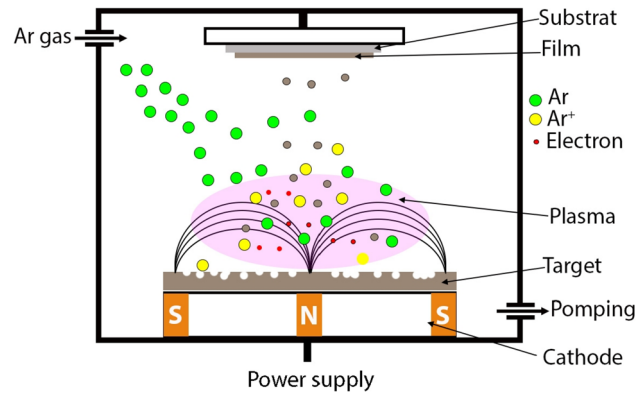


Fig. 3 Magnetron sputtering technique

target surface with a similar potential. The secondary electrons support the discharge by ionizing the argon gas (or other working gas). Thus, the produced ions bombard the target leading to the sputter of material and the generation once again of secondary electrons. In the case of a diode-type discharge and according to Paschen's law, the discharge voltage depends on the distance between the electrodes and the gas pressure. To initiate this discharge, the pressure must be high. However, this can have an important impact on the growth rate and the film quality, due to the high collision that can occur between sputtered atoms and ions in the plasma. To solve this problem, magnetron cathodes were developed to trap the electrons close to the target to increase the ionization rate of the gas and consequently the deposition rate. Magnetron sputtering can operate under low pressure. This section offers an overview of the types of targets and the various sputtering modes that have been used to fabricate HEFs through magnetron sputtering.

The coatings can be produced using targets, which may be single-phase or composite depending on how the alloy is produced in the solid state. A single-phase target consists of a single pure element. During the impact of the ions on the target surface, the element is sputtered at its own sputtering rate. In addition, the target is cooled to prevent volume diffusion. This implies the permanent expulsion of material from the target. In this case, each atom is ejected according to its own spatial distribution.

In the case of a composite target, the challenge lies in defining the ratio of the parts made up of each metal to achieve the desired coating composition. Generally, three types of targets can be proposed: concentric, mosaic, and dispersed.

The reported high-entropy films deposited by sputtering have been generated using three approaches: mosaic, dispersed multi-elements, and individual targets (Fig. 4). For example, in the case of dispersed elements, the target is fabricated through an arc-melting process [42, 43], while

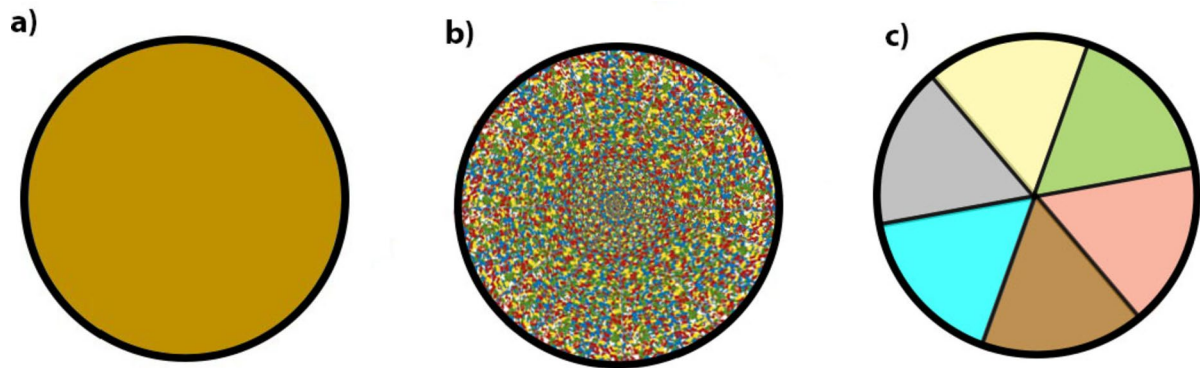


Fig. 4 Different types of targets are used to elaborate HEFs by sputtering. **a** Multi-individual pure elements. **b** One target with dispersed multi-elements. **c** Mosaic assembly

others are produced by hot-pressing a mixture of powders [44]. The individual targets are co-sputtered simultaneously to elaborate HEF. Lou et al. [45] utilizing various DC and RF generators to deposit the film. The mosaic assembly is also documented in the literature, indicating the feasibility of sputtered HEFs [46, 47].

3.1 Balanced and unbalanced magnetron sputtering

Depending on the magnet configuration, magnetron sputtering can be classified as balanced or unbalanced. In a balanced configuration, magnets with equal power ensure that all field lines pass through the central magnet, creating a closed, magnetic field where electrons are confined. In the case of the conventional magnetron sputtering, ions bombard the target in the plasma to release atoms that deposit onto the substrate. However, this process can be irregular, leading to non-uniform film thickness. Balanced magnetron sputtering addresses this issue. In this case, the substrate is not seriously affected by the ions. This is suitable for deposition on heat-sensitive substrate. To enhance ions flow toward the substrate, unbalanced magnetron was developed. This approach involves adjusting magnetic flux through one of the poles, resulting in an imbalance magnet circuit. Unbalanced magnetron sputtering has been reported in the preparation of HEFs [48–50].

3.2 DC magnetron sputtering

In the case of DCMS, the target is maintained at a constant negative voltage (or power) under argon pressure. Argon is commonly used as a working gas with a pressure varying between 0.1 and 1.5 Pa. Under these conditions, the current densities are in the order of ten mA/cm² with power densities of tens W/cm³. The process produces a plasma density in the order of 10⁻¹⁴ to 10⁻¹⁶ m⁻³ [51]. The metal

vapor is much more energetic than the thermally evaporated elements. The ionization mechanism of the target's atoms is based on Penning ionization, which occurs through the collision with argon ions (Ar⁺). The mean free path of the sputtered elements can exceed 50 cm. Most deposited HEFs, particularly RHEFs, have been produced using the DC mode in magnetron sputtering.

3.3 HiPIMS

The main limitation of conventional sputtering is the low speed and the arbitrary trajectory of the sputtered elements. This makes the control of their direction difficult, which is detrimental to the film quality. Sputtering processes have been developed to achieve a higher flow of ions than neutrals, known as ionized physical vapor deposition (IPVD). Two aspects have then been developed: complementary ionization through radio frequency (RF) or high-power impulse magnetron sputtering (HiPIMS). In the case of HiPIMS, no secondary plasma is required to ionize the vapor. Instead, the magnetron cathode is equipped with a pulse power supply capable of delivering instantaneous and high power which can reach megawatts. HiPIMS technology [52] generates very high instantaneous currents while maintaining a low target temperature. This is achieved by using short pulses ranging from a few microseconds to a few hundred microseconds.

3.4 RF magnetron sputtering

Some of HEFs have been prepared using RF magnetron sputtering [53–56]. For instance, Alam et al. [47] fabricated a mosaic target and employed RF magnetron sputtering to deposit TiMoVWCr HEFs. As the target was homemade, the magnets were geometrically arranged under the cathode (hole target) with opposite poles in order to confine

the plasma to the center. Several studies have focused on the effect of RF on HEF properties, including morphology, structure, and mechanical properties [57].

4 Microstructures and phases of RHEFs by magnetron sputtering

Recent research focuses on the development of new refractory high-entropy alloys and films. The materials consist of groups IV and VI elements in the periodic table. Their properties have been studied at room temperature and elevated temperatures. Generally, the majority of refractory high-entropy alloys are primarily composed of refractory elements from the transition group. They exhibit a body-centered cubic (bcc) structure and enhanced solubility. Xiong et al. [58] reported that RHEAs can be classified into three distinct types: bcc solid solution, precipitation of B2, and laves. Compared to the alloys, few works on the films, especially those deposited by magnetron sputtering, were reported in the literature. In this section, phases and microstructure of different RHEFs deposited by magnetron sputtering will be presented.

Xia et al. [59, 60] have reported characterizations of MoNbTaW by studying their properties under the effect of the nitrogen and the angular deposition parameters. The films were deposited by using two techniques, magnetron sputtering and arc deposition. By adding the nitrogen, a phase transformation from bcc to fcc was observed. This transformation occurred with a nitrogen content varying from 25 to 30 at.%. The study reveals that the two deposition methods have a minor effect on the growth conditions of the film's structure. Fritze et al. [61] studied the temperature effect on the evolution phase of HfNbTiVZr. The film undergoes a phase transformation from amorphous to bcc phase at 275° followed by another transformation to bcc + laves when the temperature reaches 450 °C. Similarly, Ali et al. developed octonary RHEFs consisting of strong nitrides forming elements by using the magnetron sputtering process. The increase of the nitrogen flow leads to a phase transformation from amorphous to a fcc phase. In their study, Bi et al. [62] examined NbMoTaWV films deposited by magnetron sputtering, along with their oxides (Fig. 5). The works aimed to investigate the local evolution of the structure of these films, first by weak-enthalpy-element and second under the effect of oxygen in the case of oxide. They observed that the film without oxygen exhibits a single-phase bcc structure, with three identified peaks (110), (200), and (211). However, as the oxygen content increases, the films only display a single broad diffraction suggesting the formation of amorphous or nanocrystalline structure. With advancements in microscale devices to smaller dimensions, researchers are studying newly developed high-entropy alloys that offer superior performances.

Feng et al. [63] investigated the impact of Zr element on the mechanical properties of CoCrFeNiZr_x ($x = 0, 0.3, 0.5, 1$) high-entropy alloy thin films. Concerning the structure, as the Zr concentration increased from 0 to 20.7 at.%, a transition from single-phase crystal to an amorphous structure occurred. However, with an intermediate Zr content ranging from 7.0 to 12.9 at.%, a crystal–amorphous dual-phase structure with Zr element segregation formed.

In the case of (NbMoTaW)_{100-x}V_x, the films exhibit bcc structure. When V content increases, the lattice parameter decreases. A transmission electronic microscopy analysis revealed the formation of a nanocrystalline columnar structure. Uniform grain size was reported of the films with an average of about 40 nm. For the second study, the effect of oxygen on the local evolution of (NbMoTaWV)_{100-x}O_x films was studied. The result indicates a change of the local structure from m-m14 to O-m6 after increasing the O content. Magnetron sputtering proves to be an essential method for preparing high-quality nanocrystalline high-entropy thin films. W. Liao et al. [64] investigated the CoCrFeNiAl_{0.3} film, which is composed of fcc solid solution nanocrystals with a minor content of the ordered NiAl-type bcc phase. The results indicate that the nanocrystals exhibit preferential orientation toward [64]. Further TEM analysis revealed the formation of grains with a size of 10 nm. Our group recently published a study of yttrium effect on the microstructure of TiTaZrHfW RHEF [65]. In Y-free films, an amorphous phase is formed, while new phases are formed after the addition of yttrium. In fact, TEM analysis revealed the formation of nanograins with two phases L12 and Y-P6/mmm structure. This shows the effect of yttrium when is added into RHEFs with low and high content.

The refractory film (AlTiZrHfTa)_{1-x}N_x was deposited by magnetron sputtering as a function of the nitrogen percentage ($R_{N_2} = N_2 / (Ar + N_2)$) [66]. The film without nitrogen, AlTiZrHfTa, exhibits an amorphous structure (Fig. 6a, b), while the nitrides are characterized by a NaCl-type fcc structure. Upon the addition of nitrogen, the RHEFs display a dense columnar microstructure. With an R_{N_2} percentage of 10%, the film adopts a fibrous morphology in the direction of film growth (Fig. 6c, d). In the film obtained at $R_{N_2} = 40\%$, straight columns are observed throughout the thickness of the film (Fig. 6e). This nitride demonstrates the formation of a biphasic system consisting of an amorphous phase and a crystalline phase. Indeed, the SAED diagram (Fig. 6d) reveals a diffuse ring and other discontinuities to (200), (111), and (220).

5 Mechanical properties

5.1 Hardness and Young's modulus

The mechanical properties of RHEFs have been improved by several strategies such as the effect of additive elements, the

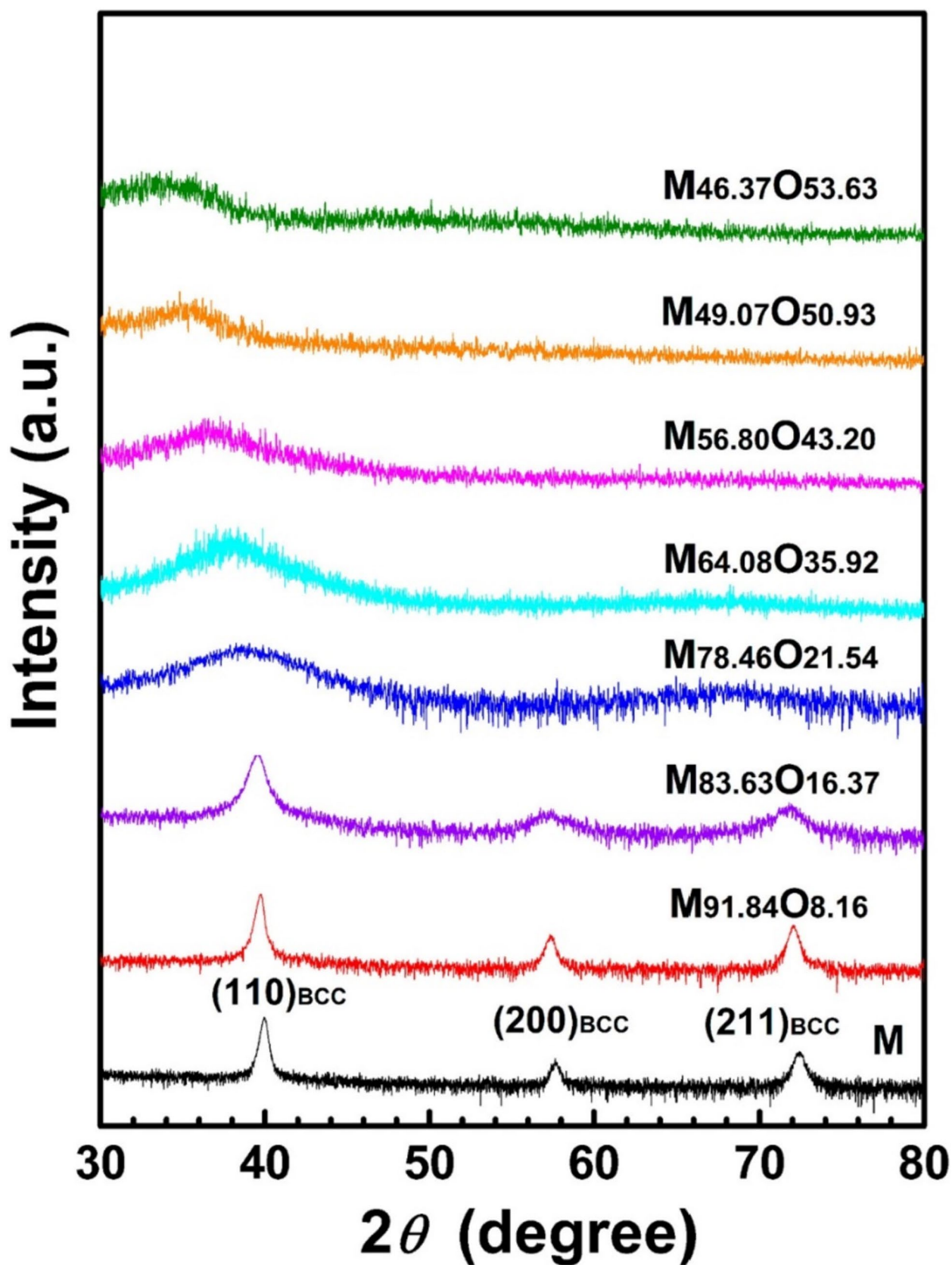
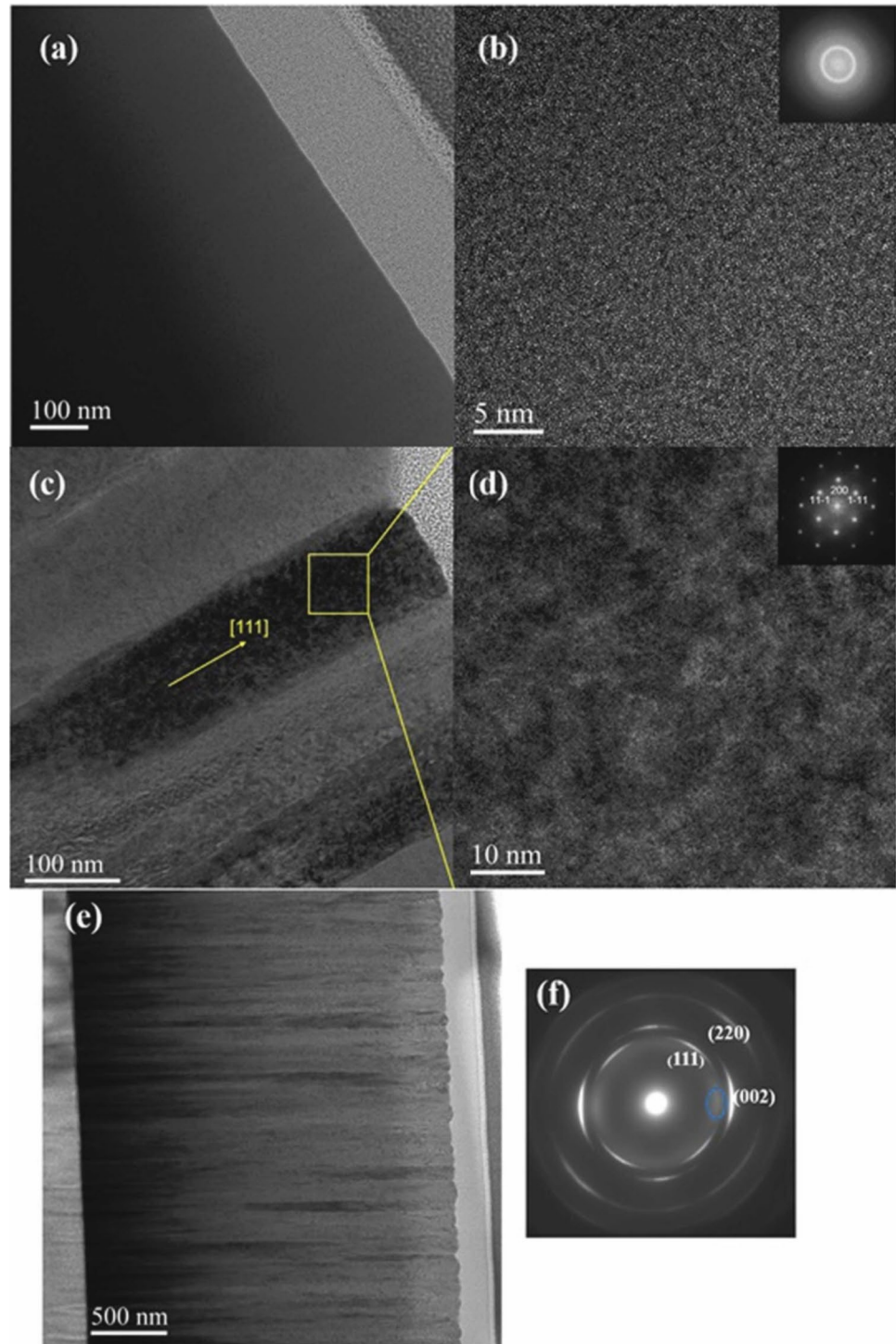


Fig. 5 GIXRD patterns of the as-deposited $M_{100-x}O_x$ ($x=0-53.63$). Figure reproduced and adapted with permission from reference [62]

Fig. 6 Bright field and HRTEM images associated SAED pattern of AlTiZrHfTa at $R_{N_2}=0\%$ (a, b), at $R_{N_2}=10\%$ (c, d), and at $R_{N_2}=40\%$ (e, f). Figure reproduced and adapted with permission from reference [66]



addition of nitrogen, the increase of the deposition temperature, and the effect of substrates bias. All these parameters strongly influence the microstructure of the films, which affect their mechanical properties. Xia et al. [59] deposited MoNbTaVW and its nitrides by direct current magnetron sputtering (DCMS) as well as cathodic arc disposition (CAD) techniques. The ratio of metal to nitrogen in the film controls

phase formation. They have reported that the formation of the fcc phase is accompanied by an increase in hardness with values of up to 30 GPa. The introduction of nitrogen led to further embrittlement of the films, as the fcc nitride phase showed a lower cracking elongation in the tensile tests carried out and thus earlier failure. The results obtained can contribute to a better understanding of the physical vapor

deposition of metallic and HEFs. Stasiak et al. [67] have studied the effect of the nitrogen on hardness of CrHfMo-TaW under two different conditions: deposition at room temperature (RT) and deposition at 750 °C. The metallic films (without nitrogen) revealed a hardness of 13.9 GPa while that of the film with 5 sccm of nitrogen was measured at 21.9 GPa (Fig. 7a). By increasing the nitrogen content, even the formation of the NaCl-type phase of high-entropy films which reported to be hard compared the free-nitrogen films, CrHfMoTaW nitrides show lower hardness. The study reveals that the hardness of the films with 10 and 20 sccm of nitrogen is lower than that of the free-nitrogen film. This could be due to the coarser structure and porosity. However, at 750 °C, a metallic bcc phase is formed. The hardness was measured at 17 GPa. With 5 sccm of nitrogen, the film has 23 GPa of hardness which is the highest value of the films investigated in different conditions. The measurements showed that the hardness of fcc nitride coatings for the series deposited at 750 °C is lower than that deposited at RT. Young's modulus, as a function of the nitrogen flow, is also reported. Experimental values in comparison with the simulation are presented in Fig. 7b. Young's modulus is 343 GPa for the pure metallic sample. However, the sample deposited under 5 sccm of nitrogen has a value of 431 GPa. Increasing the nitrogen flow from 10 to 20 sccm leads to a decrease of Young's modulus. For the metallic film produced at RT, Young's modulus is 343 GPa while that deposited under 5 sccm of nitrogen has higher Young's modulus (431 GPa). NaCl-type fcc nitride prepared at RT shows a decreasing of Young's modulus from 471 to 379 GPa when the nitrogen flow increases from 10 to 20 sccm. For a metallic deposited at HT, it has a bcc phase and presents a Young's modulus of 404 GPa. At low nitrogen flow (5 sccm), 487 GPa for Young's modulus compared to for fcc-based film obtained at 10 sccm.

Cheng et al. [68] have produced two RHEFs by co-sputtering Mo or W with TiZrHfNbTa. The addition of Mo or

W in the film leads to hardness increasing. TiZrHfNbTaW film shows a higher hardness compared to that of TiZrHfNbTaMo and TiZrHfNbTa. The addition of such elements conduces to a higher strengthening effect. The study reports the formation of small Mo or W-rich nanocrystallites that leads to reinforcement of the matrix leading to improved hardness. However, quasi-similar elastic modulus was obtained for all films. Improved hardness and elastic modulus were reported by Zhan et al. [69] in the case of NbTiZr refractory medium film by adding silicon (Si). The Si-free film shows a hardness and Young's modulus of 2.2 GPa and 62.6 GPa respectively. Higher values were obtained after the addition of Si. With 25 at.% of Si, the hardness was measured at 5.1 GPa and Young's modulus at 105.1 GPa. As reported by the study, the improvement of the mechanical properties of these films could be due to the increase in hybridized metal-metalloid bonding that is consistent with CALPHAD data. On the other hand, Feng et al. [67] studied the effect of grain size and the thickness of the films on their mechanical properties. They showed that NbMoTaW film having a grain size of 10 nm and a thickness of 250 nm presents an improved hardness.

On the other hand, $(Al_{0.5}CrFeNiTi_{0.25})N_x$ high-entropy films were produced using reactive direct current magnetron sputtering in reactive mode [70]. With an increase in nitrogen concentration, the hardness and Young's modulus of the films showed an upward trend. The highest values for hardness and Young's modulus were measured at 21.78 GPa and 253.8 GPa, respectively. Liao et al. [71] studied $Al_{0.3}CoCrFeNi$ films, focusing on their micromechanical properties. The thin film, prepared by magnetron sputtering, is smooth with a roughness of 5 nm. To further investigate the micromechanical properties, films with a diameter of 738 nm were prepared, and compression tests were performed. The measured hardness and yield strength were 11.09 GPa and 1024 MPa, respectively, which are about three times higher than those of bulk sample. Cemin et al.

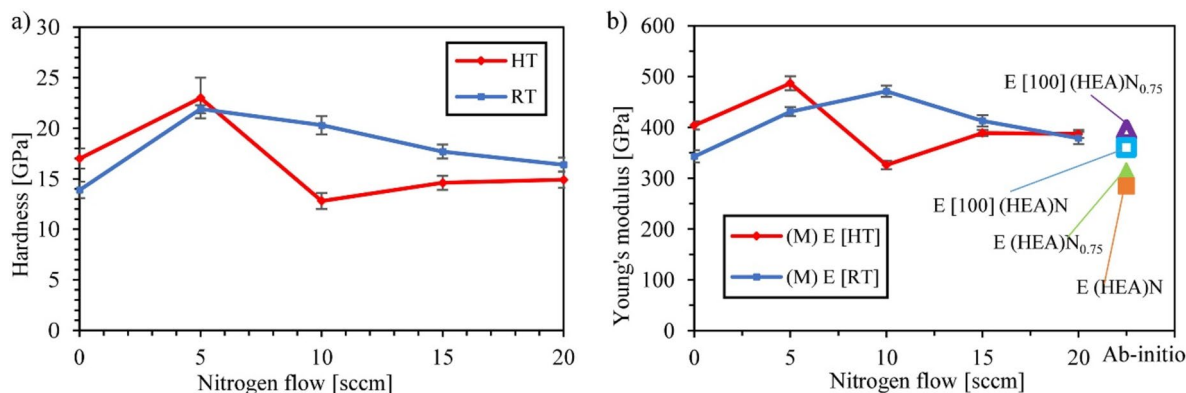


Fig. 7 Hardness (a) and Young's modulus (b) of films, as a function of nitrogen flow, deposited at RT and HT (750 °C). Figure reproduced and modified with permission of reference [67]

[72] have reported the effect of substrate bias on the mechanical properties of NbTaTiVZr RHEF. The film was deposited by magnetron sputtering at 400 °C. The hardness increased from 6.5 to 8.3 GPa when the substrate bias increased from 0 to –75 V whereas the reduced modulus showed minor changes. The study reports that the hardening effect of the films as a function of the substrate bias could be due to the refining of the grain size (Hall Petch effect). A similar study was reported by Wang et al. [73] showing the improved mechanical properties of ZrNbTiMo film as a function of substrate bias (Fig. 8). With increasing substrate bias, hardness and Young's modulus increase continuously, reaching 21.3 GPa and 231.0 GPa respectively at –200 V. The authors report that this trend, particularly in the case of hardness of ZrNbTiMo films, is due to crystalline microstructure effect. The temperature has also a strong effect on the mechanical properties of the RHEFs. TaNbHfZr film was deposited at three different temperatures 25, 500, and 700 °C. The amorphous phase formed at 25 °C shows a hardness of 8 GPa while a crystalline formed at 700 °C has 15.3 GPa. The reduced modulus increased from 94.5 to 183.6 GPa with temperature increasing. Solid-solution and grain boundary

strengthening could be the reasons for the improved mechanical properties of TaNbHfZr RHEFs.

5.2 Wear resistance

ZrNbTiMo RHEFs were fabricated by DCMS on ASTM304 for tribological property tests. Liu et al. [74] performed the friction analysis using a constant load of 2N and for 30 min. The results are given as a function of the sputtering power. A fluctuation of the friction coefficient was reported due to the irregular morphology of the film caused by the pits, plastic deformation, and debris particles (Fig. 9). Four films prepared with a sputtering power varying from 90 to 180 W (splicing target: $\varnothing 76.2 \times 5 \text{ mm}^2$) revealing the best wear resistance of the that obtained at 150 W. Regarding the wear mechanism, two films were tested and demonstrated an abrasive wear behavior. Fatigue cracks occurred on its surface due to the repeated plastic deformation during the test. According to the results, the film obtained with 150 W revealed a maximum toughness ($0.437 \text{ MPa} \times \text{m}^{1/2}$) and best wear rate $5.22 \times 10^{-7} \text{ mm}^3/\text{N.m}$.

The effect of the temperature on the tribological properties of RHEFs has been studied by Xing et al. [75]. The

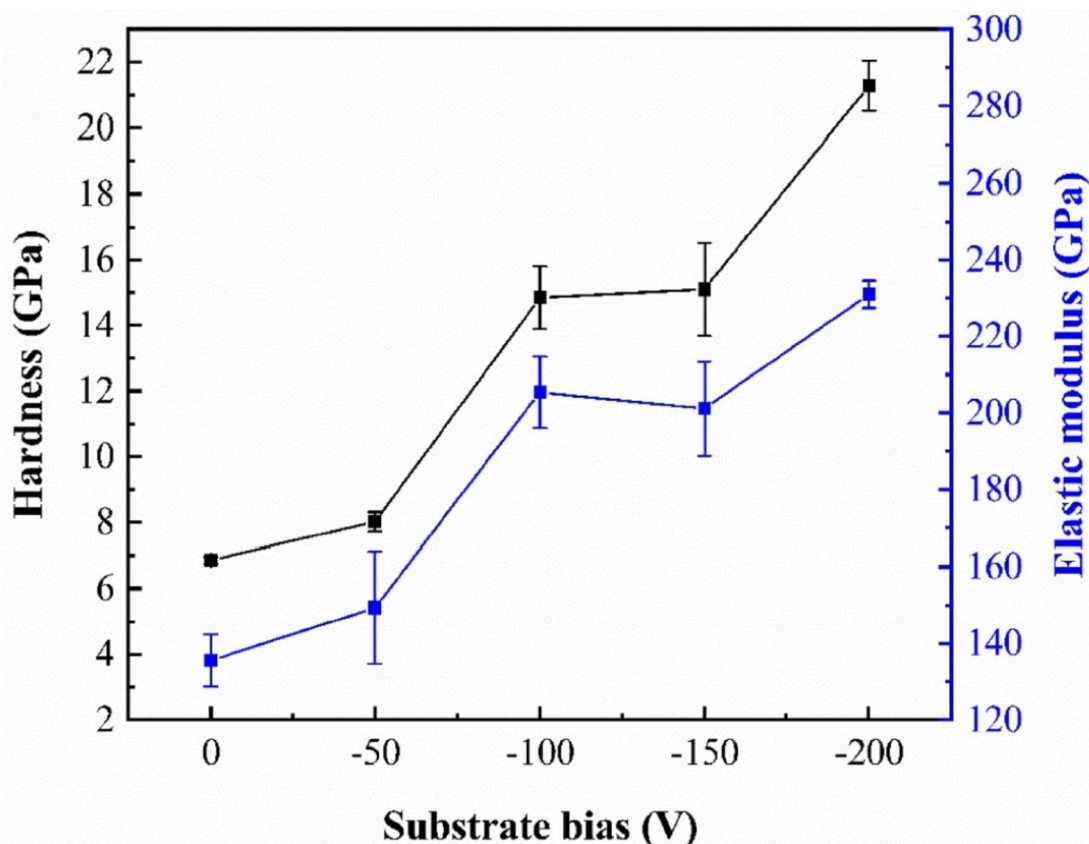


Fig. 8 Hardness and Young's modulus of ZrNbTiMo film under different substrate biases. Figure reproduced and modified with permission of reference [73]

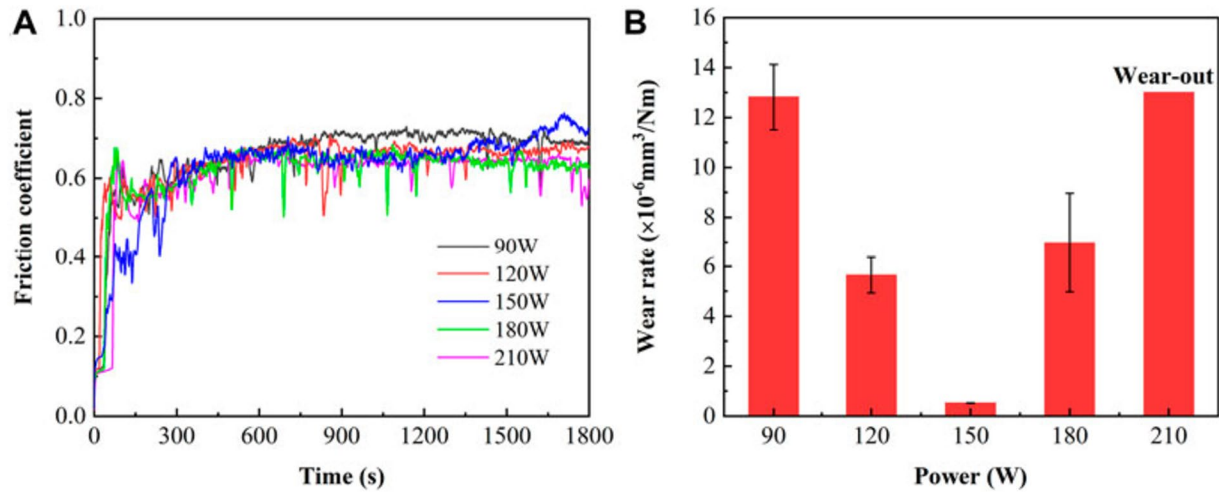


Fig. 9 **A** Friction coefficient curve and **B** wear rate of the ZrNbTiMo RHEA films deposited at different sputtering power. Figure reproduced and modified with permission of reference [74]

friction coefficient at room temperature was twice that of steel substrate (SS) due to the delamination processes. An oxide layer formed on film at 300 °C leads to a decrease of the friction coefficient. The oxide plays the role of a lubricant to reduce the wear effect. However, as the temperature increases, the friction coefficient increases for the film and SS. By comparing these two substrates, the authors showed that even the wear rate increases by increasing the temperature is still lower than that of SS.

6 Functional properties

6.1 Oxidation of RHEFs

In recent years, the rapid development of aerospace and other material used at elevated temperatures requires excellent mechanical properties as well as high oxidation resistance. The elements tend to form loose oxides upon the increase of the temperature. The oxygen diffusion process becomes contentious as a function of the temperature. Given such an environment, RHEFs must be resistant to oxidation at elevated temperatures to provide materials operating under severe conditions. In the case of refractory high-entropy alloys, the addition of some elements such as Al, Si, and Cr has been found relevant to improve the oxidation resistance. Protective layers Al_2O_3 , SiO_3 , and Cr_2O_3 can be formed respectively on the surface of the alloys acting as diffusion barrier of the oxygen.

In the case of coatings, few studies of RHEFs are reported in the literature. Liao et al. [76] have studied the oxidation of WNbMoTaVO. The films have been deposited by using DCMS. The study revealed no change in the microstructure

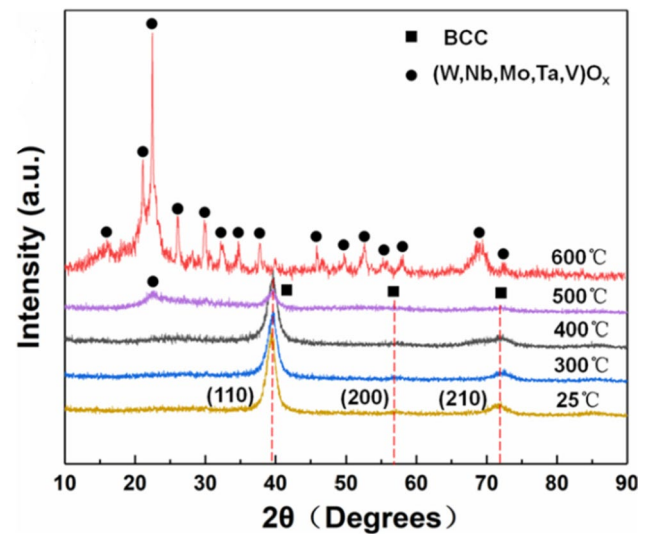


Fig. 10 XRD diffractograms of WNbMoTaVO films after oxidation at different temperatures. Figure reproduced and modified with permission of reference [76]

of the films below 400 °C (Fig. 10). However, when the temperature reaches 600 °C, a crystalline structure is observed. The formation of oxides was started at 400 °C and became complete when the temperature increased to 600 °C. Various binary oxides were generated at 600 °C. At low temperatures, the growth of oxides has been reported to be slowed down due to sluggish diffusion. The favored diffusion of the atoms leads to the acceleration of the oxidation process.

Recently, Bouissil et al. [77] investigated TiTaZrHfW magnetron sputtered films and reported a medium oxidation resistance. Using TGA, the oxidation behavior of the metallic and the nitride films at different temperatures

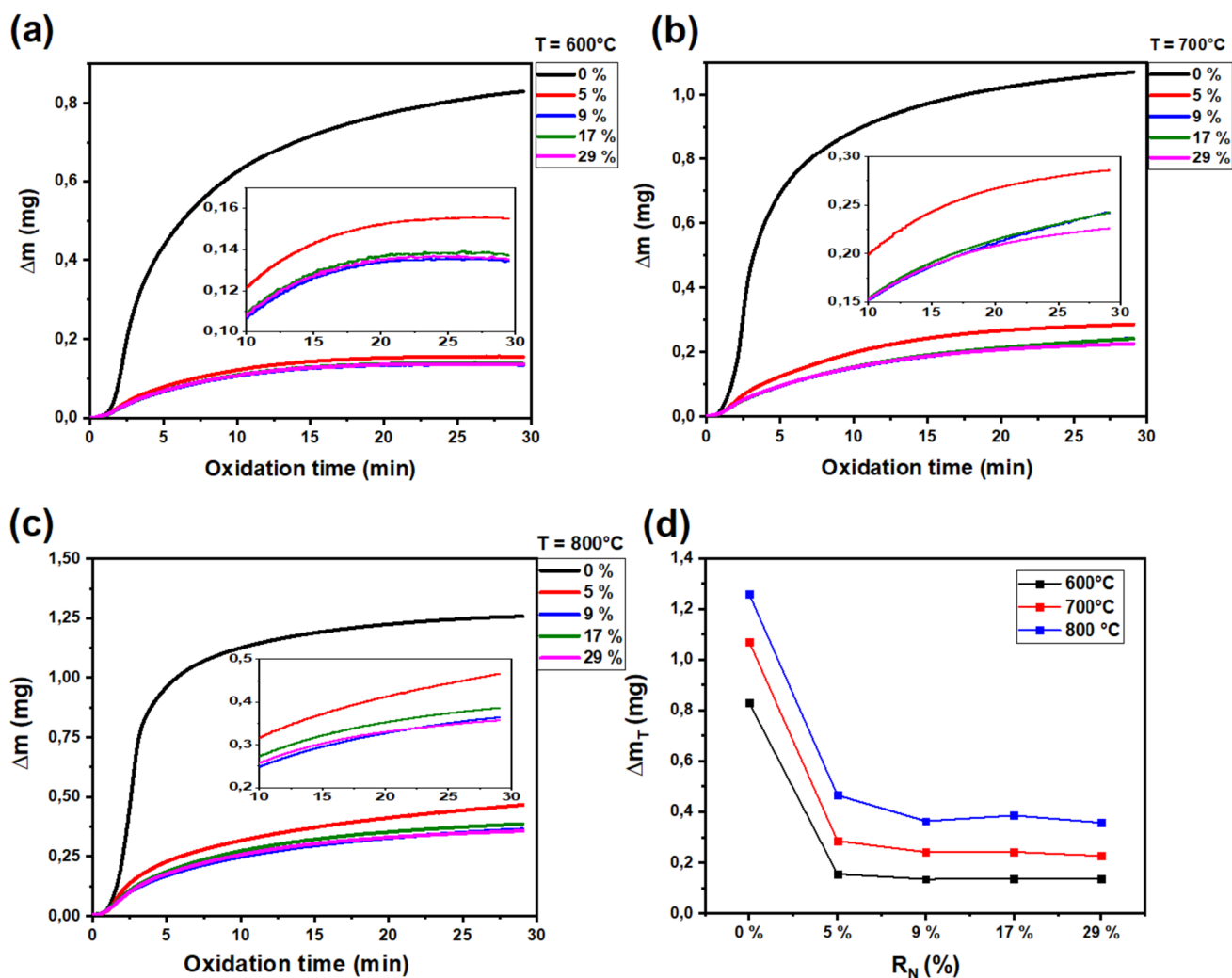


Fig. 11 Weight gain of TiTaZrHfW(-N) films per ΔS at 600 (a), 700 (b), 800 °C (c), and total weight gain as a function of the nitrogen flow rate at different temperatures (d). Figure reproduced and modified with permission of reference [77]

(600, 700, and 800 °C), the weight gain per surface area was measured (Fig. 11). Compared to metallic film, the nitrides at different nitrogen flow rates show lower weight gain. However, as the temperature increases, the weight gain increases in the case of these nitrides. The authors have calculated the oxidation rate constant (k_p) and the activation energy (E_a). At 800 °C, the lower k_p and the high value of E_a were found for the nitride deposited at nitrogen flow of 9% at $8 \times 10^{-5} \text{ mg}^2/\text{cm}^4 \cdot \text{s}^{-1}$ and 102 kJ mol^{-1} , respectively. The improvement of the oxidation resistance in the case of nitride could be due to the formation of the metal nitrogen covalent bonds which make the metal less reactive with the oxygen. The study reveals the medium oxidation resistance of TiTaZrHfW(-N) compared to some reported works. These works were believed to be in connection with (i) a strong affinity of refractory elements like Ti, Zr, and Hf with oxygen and the low adhesion of

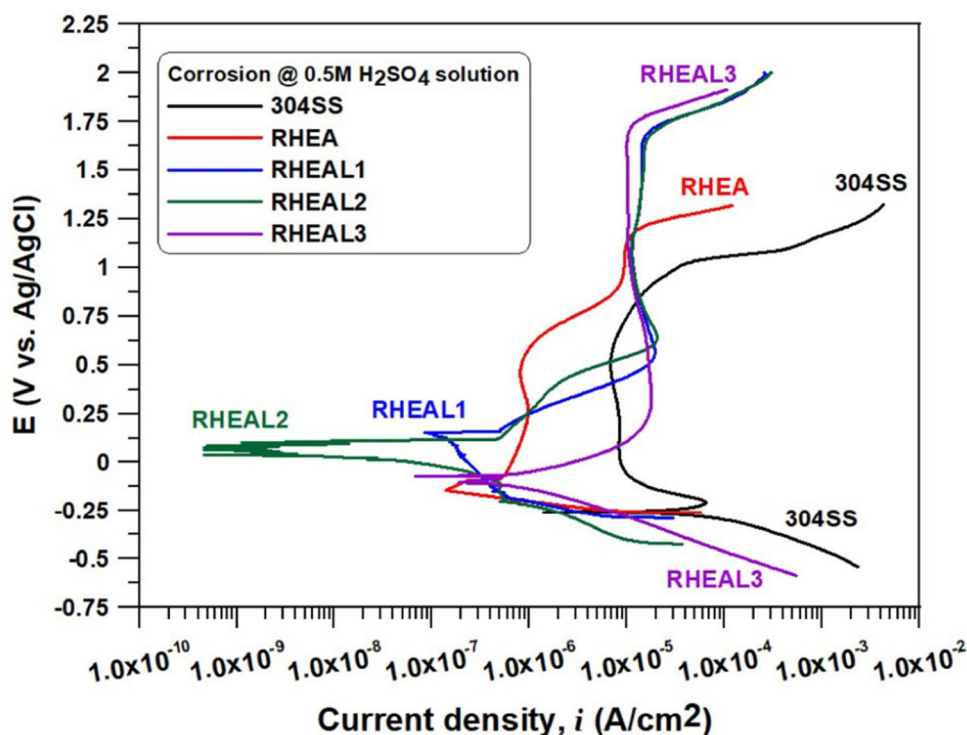
their oxides to metal; (ii) the formation of cracked and porous oxides resulting from a low boiling temperature of W-oxides.

6.2 Electrochemical measurements of RHEFs

The corrosion resistance of a material can be estimated by measuring the corrosion current (I_{corr}) and the corrosion potential (E_{corr}) from electrochemical conventional experiments. These parameters must be calculated from the TAFEL line analysis. The corrosion resistance is inversely proportional to the product of I_{corr} and E_{corr} .

Concerning RHEFs, Banachi et al. [78] have studied the corrosion behavior of VNbMoTaWAl in 0.5 M H_2SO_4 solution (Fig. 12). The films were prepared by pulsed DC magnetron sputtering technique and the Al effect on the properties of films has been investigated. The results reveal a wider

Fig. 12 Potentiodynamic polarization curve of VNbMoTaWAl RHEFs as a function of Al content compared to that of 304L stainless steel in 0.5 M H₂SO₄ solution. Figure reproduced and modified with permission of reference [78]



passivation range of substrate RHEFs compared to that of 304SS substrate (Fig. 12). I_{corr} decreased from 2.62 to 0.43 $\mu\text{A}/\text{cm}^2$ when the film was deposited on the steel. The addition of Al leads to a denser film that plays a crucial role in the corrosion resistance improvement. A higher corrosion resistance was calculated at 768.74 $\Omega\text{ cm}^2$ for the film with 2.37 at.% of Al.

Alamdari et al. [79] have studied the corrosion behavior of Ti_{1.5}ZrTa_{0.5}Nb_{0.5}W_{0.5} RHEFs in phosphate buffer saline (PBS) solution at 37 °C. The results were compared with those of Ti6Al4V samples. The objective was to analyze the biocorrosion of the RHEFs in simulated human body conditions. For that, the authors have studied undoped and Ag-doped RHEFs. Compared to Ti6Al4V substrate that has a potential higher than 1.4 V, both undoped and Ag-doped RHEFs present continuous passivation plateau without pitting effect revealing good corrosion resistance. To further analyze the corrosion behavior of these films, the authors calculated their protective efficiency. They found that the Ag-doped RHEF presents the highest protective efficiency due to its lower porosity. Ag particles are seen as corrosion inhibitors.

Other Ti_{1.5}ZrTa_{0.5}Nb_{0.5}Hf_{0.5} RHEFs have been studied to evaluate their corrosion behavior in PBS solution. The study focused on the biocompatibility of these refractory films deposited by RF magnetron sputtering on three different biomedical 316L, CoCrMo, and Ti6Al4V substrates. The results revealed good corrosion resistance of the coated compared to uncoated substrates. Moreover, the

coated Ti6Al4V substrate by RHEFs showed a continuous passivation plateau and low I_{corr} . The same group revealed a non-cytotoxic character of both undoped and Ag-doped Ti_{1.5}ZrTa_{0.5}Nb_{0.5}W_{0.5} RHEFs [79]. Due to their properties, the film can be seen as a good candidate for developing biocompatible antibacterial coating.

The medium entropy alloys have also attracted more attention during these last years. Lou et al. have studied the corrosion behavior of refractory WNbTaTi medium entropy thin film and its nitride. The measurements were done in 5 wt% NaCl solution. By comparing the analysis to 304 stainless steel substrates, the results show a good corrosion resistance of nitrogen-free W_{37.9}Nb_{25.8}Ta_{28.8}Ti_{7.5}. The film has a low I_{corr} 1.59 $\times 10^{-2}$ $\mu\text{A cm}^{-2}$, the highest polarization resistance of 1400.8 $\text{k}\Omega\text{ cm}^2$, and a large passivation range of 1.132 V. The good corrosion resistance of the film is due to the presence of a large amount of Ta and Nb known to resist corrosion and high configurational entropy as reported by authors. C.-S. Feng et al. [80] reported a study of a new high-entropy WNbMoTaV thin film. The film is characterized by an amorphous structure and features, a smooth surface with low height variation. Its electrical resistivity was measured at 320.6 $\mu\Omega\text{ cm}$ with a low current density of 0.088 A cm^{-2} . The film's corrosion resistance at room temperature has been shown to be superior to that of the conventional AISI 316L stainless steel. The measurements were performed in 3.5 wt% NaCl solution. The

corrosion potential is measured at -0.225 V, and the corrosion current density is about $0.088 \mu\text{A cm}^{-2}$, which is lower than that of steel.

6.3 Irradiation resistance of RHEFs

RHEFs have also been investigated for nuclear applications. Xe ions have been used to irradiate the films. For example, El-Atwani et al. [81] have investigated the irradiation resistance of the film WTaVCr deposited by using the magnetron sputtering technique. Negligible irradiation hardening and no sign of radiation-induced dislocations were reported after irradiating the film at RT and 800°C . Wang et al. [82] have studied the TiZrNbTaV and its nitride by irradiating the films using Xe-ions at RT and 500°C . The irradiation conditions were inspired by the nuclear fuel assemblies in the most pressure water nuclear reactors. A 3 MeV-Xe ion irradiation was carried out on the films for a duration of 2.5 h at RT and 500°C . No change was observed in both metallic and nitride films at RT. At 500°C , the irradiated nitride film remains intact under the irradiation effect compared to the metallic film. The latter undergoes a phase transformation from amorphous to bcc under Xe ion irradiation. Equiaxed grains with a diameter of 5–10 nm were formed near the film's surface compared to the grain size of 14 nm formed near the substrate. In the case of nitride, excellent irradiation resistance was observed in such conditions. Similarly, Pu et al. [83] reported on the irradiation effect on TaTiWCr RHEF and W film. H^+ with a fluence ranging from $1 \times 10^{16} \text{ cm}^{-2}$ to $2 \times 10^{17} \text{ cm}^{-2}$ was used. Crystallization phenomenon occurred in the RHEF at a fluence of 5×10^{16} . As the fluence increases, the grain size of RHEF also increases and was estimated at 8 nm for a fluence of $1 \times 10^{17} \text{ cm}^{-2}$ and 14 nm for a fluence of $2 \times 10^{17} \text{ cm}^{-2}$. The authors revealed that even with the easy crystallization of TaTiWCr RHEF under the irradiation effect, it has a good swelling resistance compared to that of W film.

6.4 Electrical properties of RHEFs

Regarding the development of nanofabricated electronic devices, the investigation of electrical properties of high-entropy films has attracted more attention in the last few years. Kim et al. [44] have studied the mechanical and electrical properties of NbMoTaW RHEF. The film was deposited by the magnetron sputtering technique. The study focuses on the comparison of the electrical properties of the film compared to those pure individual element films as a function of grain size. Generally, electrical resistivity is related to lattice distortion as well as microstructural defects such as dislocations and vacancies. Due to the severe lattice distortion, NbMoTaW RHEF exhibits a high electrical

resistivity compared to that of pure refractory elements as reported by the authors.

Chen et al. [84] were interested in the study of the electrical properties of VNbMoTaW RHEF as a function of annealing temperature. The measurements were carried out on $\text{V}_{19.2}\text{Nb}_{19.4}\text{Mo}_{20.3}\text{Ta}_{19.5}\text{W}_{21.6}$ film deposited on sapphire and 304 stainless steel substrates before and after oxidation by varying the temperature from 300 to 700°C . The results show an increase of the electrical resistivity from $3.27 \times 10^{-5} \Omega \text{ cm}$ to $1.29 \times 10^{-3} \Omega \text{ cm}$ of the film deposited on sapphire after oxidation from 300 to 500°C (Fig. 13). However, the study revealed a lower electrical resistivity of the film deposited on 304 stainless steels compared to that on the sapphire substrate.

6.5 Nanolattice and nanostructures

L. Gao et al. [85] successfully demonstrated 3D hybrid nanorods coated with high-entropy alloys ($\text{CoCrFeNiAl}_{0.3}$) using RF sputtering (Fig. 14). These nanogrids range in size from 5 to 20 nm, as illustrated in Fig. 15. The study focuses on the mechanical properties of these nanorods. Employing two approaches: in situ SEM compression testing and the finite element method. SEM analysis revealed that the composite nanorods exhibit high compressive strength of $0.032 \text{ MPa kg}^{-1} \text{ m}^{-3}$ with a density well below 1000 kg m^{-3} . These materials demonstrate a reasonably good compressive capacity due to their composite nature, opening new prospects for potential applications in structural engineering, flexible electronics, and biomedical applications. The nanocrystalline structure can be considered an asset to improve the performances of the high-entropy films. For example, C. Feng et al. [86] reported that the excellent mechanical properties of (AlTiVCr)N nitride result from synergistic effect of the nanocrystalline structure, covalent bonds formed between the metallic elements and nitrogen, and interstitial strengthening.

7 Computational prediction of HEFs

The calculation-driven design of single-phase HEFs is a crucial step that enhances the exploration of various potential combinations for creating high-entropy materials, as well as predicting their microstructures and properties. This step is particularly important before embarking on costly experimental trials and errors, given that this field is still striving to reach a stage of maturity. In the following sections, we delve into three major approaches to achieve this goal: density functional theory (DFT), ab initio modeling, and calculation of phase diagrams (CALPHAD).

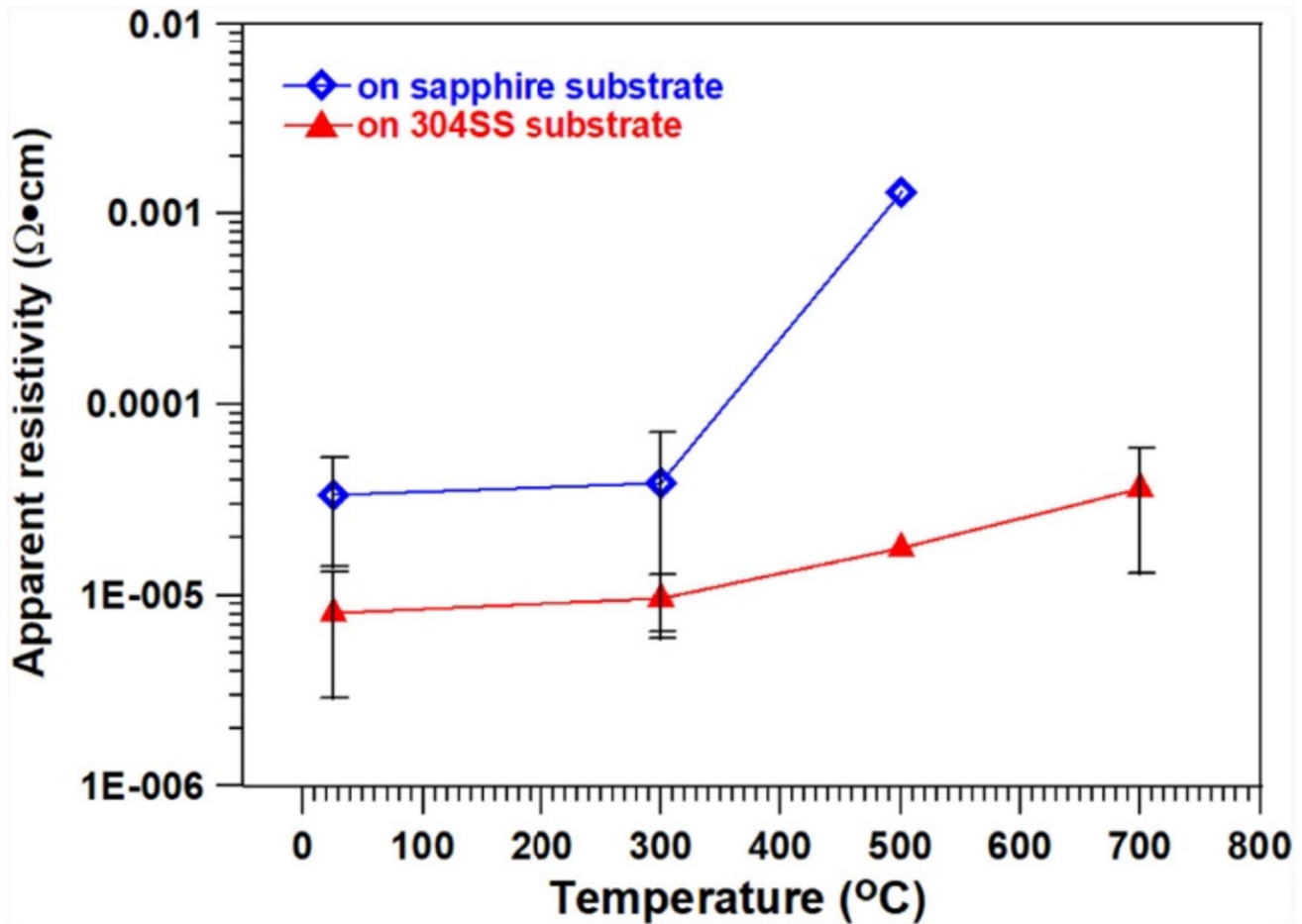


Fig. 13 Electrical resistivity of NbMoTaW RHEA thin film compared to individual refractory metals. Figure reproduced and modified with permission of reference [84]

7.1 Modeling from first principles

The behavior of particles composing any material is fully described by Schrödinger's time-independent non-relativistic wave function equation, established in 1926 [22]:

$$H \psi(r, t) = E \psi(r, t) \quad (6)$$

i.e.,

$$\frac{-\hbar^2}{2m} \nabla^2 \psi(\vec{r}, t) + V(\vec{r}, t) \psi(\vec{r}, t) = i\hbar \frac{\partial \psi(\vec{r}, t)}{\partial t} \quad (7)$$

where H represents the Hamiltonian operator, \hbar denotes the reduced Planck constant, and $\psi(r, t)$ signifies the wave-function that encapsulates all information about the system of particles. This function is complex and defined at every point in space r and time t . The solutions of the Hamiltonian denoted as En correspond to eigenvalues associated with the system. Additionally, m represents the mass of the particle

(such as electron, proton), V represents the potential arising from the surroundings, and ∇ represents the Del operator.

It is interesting to note that despite the success of quantum mechanics in correctly describing the microcosm behavior, the computation cost is impressively high. In his paper, Erwin Schrödinger [22] solved analytically hydrogen atoms composed of only an isolated electron and a proton. Beyond this simplistic system, numerical computation is the only option. Besides being challenging, it is computationally expensive and in some cases lasts more than the age of the universe. According to Paul Dirac, the real challenge is solely that the rigorous application of those laws results in extremely complicated equations to be soluble.

7.2 The adiabatic Born–Oppenheimer approximation

In the absence of electric and magnetic fields, the Hamiltonian for the Schrödinger equation above describing a material consisting of N electrons and M nuclei reads:

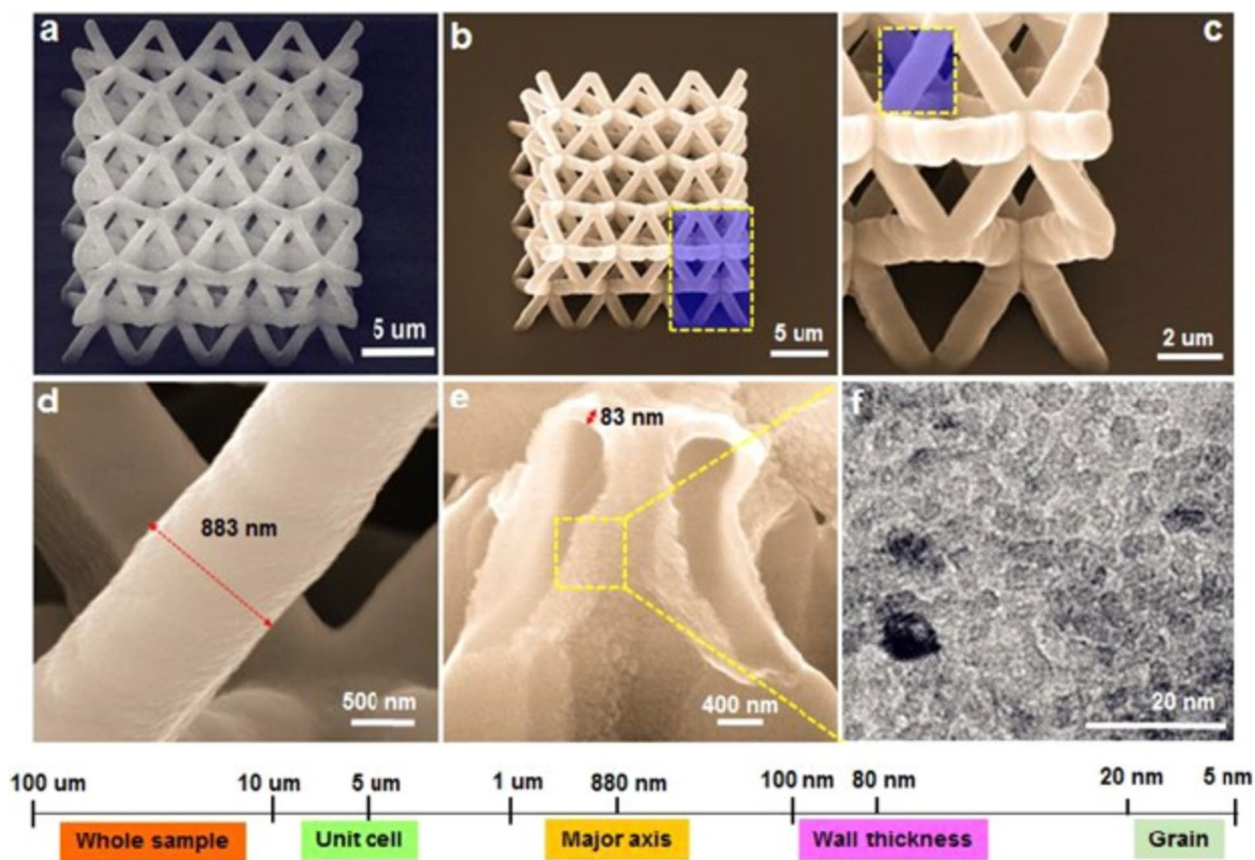


Fig. 14 Structure of composite nanolattice. **a** Primary polymer nanolattice. **b** Nanolattice coated with HEA thin film and **c**, **d** a single strut with 883 nm in diameter. **e** The thickness of the HEA is about

80 nm. **f** TEM images of the HEA with 5–20-nm grain size. Figure reproduced and modified with permission of reference [85]

Fully Non-Local

Hybrid Meta GGA

Meta GGA

GGA

LDA

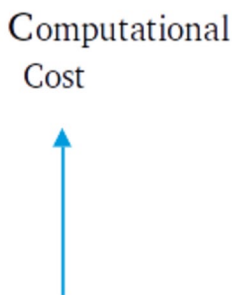


Fig. 15 The conceptual framework of Jacob’s ladder. The figure has been adapted and modified from reference [90]. J. Perdew, incorporating changes to better align with the context

$$\begin{aligned}
 H = & - \sum_{i=1}^N \frac{\hbar^2}{2m_i} \nabla^2 - \sum_{j=1}^M \frac{\hbar^2}{2m_j} \nabla^2 - \sum_{i=1}^N \sum_{j=1}^M \frac{Z_A Z_A}{r_{iA} r_{iA}} \\
 & + \sum_{i=1}^N \sum_{k>l}^M \frac{1}{r_{ij}} + \sum_{A=1}^M \sum_{B>A}^M \frac{Z_A Z_B}{R_{AB}}
 \end{aligned}
 \tag{8}$$

where r_i is the electron coordinates, r_j is the nuclei coordinates, and Z represents the atomic numbers. Electrons are denoted by lowercase subscripts and nuclei, with charge Z_i and mass M_j denoted by uppercase subscripts.

The components from left to right express electronic kinetic energy, nucleus kinetic energy, nucleus-electronic attraction, electronic-electronic repulsion, and nucleus-nucleus repulsion, respectively.

This complex Hamiltonian is simplified by the adiabatic Born-Oppenheimer approximation [23] due to the high magnitude of nucleus mass compared to electron mass. From the electron perspective, nucleus positions are static in the nucleus referential framework. Furthermore, the electrons

instantaneously readjust to nuclei motion; hence, the electrons and nuclei wave functions decouple. The new Hamiltonian is then formulated as:

$$H_e = - \sum_{i=1}^N \frac{\hbar^2}{2m_i} \nabla^2 - \sum_{i=1}^N \sum_{j=1}^M \frac{Z_A}{r_{iA}} \frac{Z_A}{r_{iA}} + \sum_{i=1}^N \sum_{k>1}^M \frac{1}{r_{ij}} \quad (9)$$

Since the nucleus kinetic energy is neglected and the nucleus-nucleus is a constant, the wave function is a function of only electron positions.

In 1964, Hohenberg and Kohn introduced two theorems [24] followed by the Kohn-Sham formulation a year later [87]. These theorems stated that the ground-state total energy of a system of interacting electrons is a unique functional of electron density. They identified the variational principle, thereby reducing the problem to computing the ground-state energy of independent electrons under an external potential—illustrated by the nuclei’s interaction with electrons. Minimizing the functional of the three-dimensional charge density is computationally less expensive than dealing with the three-dimensional wave function in a system of N electrons.

Essentially, the concept of a fictitious “jellium”—a uniform electron gas in infinite space with evenly distributed positive charges—was initially introduced by Thomas-Fermi [19, 88].

The significance of this milestone lies in the shift from computing material properties based on the wave function—a $4N$ -dimensional entity (accounting for N electrons and their spin states)—to the charge density, a simpler 3-dimensional concept. For a material with N electrons, this transition offers a substantial reduction in computational complexity. The Kohn-Sham framework exemplifies this shift, demonstrating that the challenge of modeling many-body interacting electrons within an external potential is transformed into a problem of non-interacting electrons. This transformation is showcased in the self-consistent field calculation of a set of Kohn-Sham equations, which are modifications of the Schrödinger equations.

Although they are not precisely defined, various approximations for the exchange-correlation functional have been suggested. These include the local density approximation (LDA), generalized gradient approximations (GGA), meta-GGA, and hybrid functional. These approximations aim to address the transition from a many-body interacting system to independent-electron, accounting for various quantum effects. The choice of functional relies on the charge density and generally, though not necessarily, the accuracy of calculations improves following Jacob’s ladder of approximations [89].

7.3 Pseudopotential

The primary objective of density functional theory is to minimize the computational cost of all-electron

calculations. To tackle this, Enrico Fermi [90] proposed a solution in 1934, followed by Hellman [19] a year later. Their contributions distinguished between the effects of valence electrons and core electron contributions in solving the Schrödinger equation. Since material properties are predominantly influenced by valence electrons, the effective potential considers the screening effect of inner core electrons on the valence electrons. The underlying idea is to replace the nucleus’s Coulomb attraction with a smoother potential. This led to the introduction of the pseudopotential concept, which captures the dominant effect of valence charge density. Generally, using norm-conserving, ultra-soft, and projector-augmented wave potentials for computation helps achieve varying levels of accuracy in predicting material properties, all while significantly reducing computational time.

Modern computational materials modeling, often starting from *ab initio*, employs a blend of theoretical and computational techniques, prominently including DFT. First principles approaches have garnered renown for their remarkable ability to investigate compound stability [91–94] and, in a high computational cost regime, explore temperature effects from a bottom-up perspective. The universality of DFT, underscored by its simplicity, reliability, and transferability, contributes significantly to its popularity among researchers in the field of materials science.

DFT computations offer relatively accurate enthalpy values for compounds. However, taking these data to the next level of applicability requires the $\Delta H - \delta$ rule [95]. Even when employed, this rule lacks significant physical relevance, particularly in the context of inter-metallic-based compounds.

The milestone was reached in the works of Troparvesky et al. [96] by introducing the following criterion:

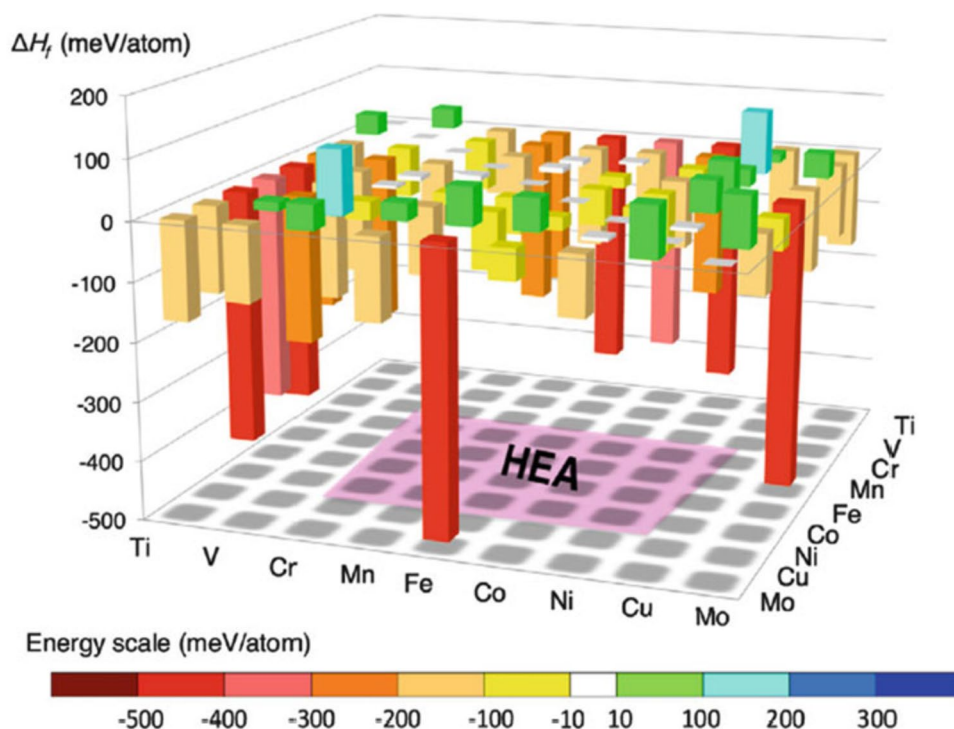
$$-RT_c \sum x_i \log x_i \geq |H_{ij}|_{\max} \quad (10)$$

where T_c represents the critical temperature, and H_{ij} denotes the absolute enthalpy value of the most stable binary compound that constitutes the system.

In 2013, thermodynamic properties were employed to compute six alloys. The data, once calculated by adding the Troparvesky et al. criterion, demonstrated enhanced significance. It was discovered that out of the six compounds studied, only CoCrFeMnNi fulfilled this criterion. The results obtained from DFT computations, as reported by Troparvesky et al. [96], are depicted in Fig. 16.

It is worth noting that the smaller values obtained by the DFT strategy for the global number of possible equimolar single-phase HEF compositions are not surprising [96]. In contrast to solving Schrödinger equations to obtain actual eigenvalues and eigenvectors, the DFT relies on Kohn-Sham modified equations, where the resulting eigenvalues

Fig. 16 DFT computation [92] of the enthalpies of formation for binary compounds. The figure has been reproduced and modified with permission of the main author of the reference [96]



and eigenvectors might not always hold clear physical significance. Among the notable weaknesses of density functional theory is its struggle to provide accurate band gap predictions for semiconductors, for example.

7.4 Calculation of the phase diagram (CALPHAD)

CALPHAD is an approach based on providing Gibbs energy values corresponding to each phase within the system. It combines the results of DFT computations with temperature-dependent semi-empirical equations for designing high-entropy alloys (HEFs). This method has been applied in numerous studies [19, 90–93, 97] facilitating the differentiation of solid solution phases, inter-metallic phases, and their combinations. A significant finding from these investigations is that the contribution of the solid solution phase to the entire system is inversely proportional to the amount of the principal elements. Similarly, the fraction of the solid solution combined with the inter-metallic phase follows a similar variation [22]. More details and database tables are available in this book [96]. It is important to note that in the absence of CALPHAD data or if the obtained results are not in line with experimental measurements, the phase diagram inspector becomes the sole alternative.

7.5 Ab initio modeling

The goal is to organize the growth of solid solutions by uncovering privileged inter-atomic bonding without

incurring extensive computational costs. It is important to note that there is no need to delve deeply into empirical interaction potentials. Numerous scientific studies have employed an efficient computational approach, utilizing the VASP commercial package [98, 99]. Researchers have also utilized similar plane-wave sets suitable for analyzing periodic systems, such as WIEN2K, another commercially available software, as well as the open-source Quantum Espresso. Moreover, certain investigations have utilized local basis set-based software, such as the commercial Gaussian and the freely available Orca software, which are primarily designed for molecular computations.

The VASP package [98, 99] has found widespread use in first-principles electronic structure calculations, delivering accurate results across a diverse range of materials. Another commercial software, WIEN2K, has been extensively employed for investigating periodic systems, particularly those with complex crystal structures. Its robust capabilities and accuracy in handling periodic boundary conditions [100–103] make it a favored choice. Additionally, Quantum Espresso, an open-source package, has gained popularity for the study of periodic systems and has made substantial contributions to the scientific community [104].

Furthermore, local basis set-based software, such as Gaussian [105, 106], has proven to be valuable for molecular computations, including molecular dynamics simulations and accurate quantum chemical calculations. On the other hand, Orca, a freely available software, has gained

recognition for its capabilities in performing high-level computations on molecular systems [107–110].

These computational tools and methods have played an indispensable role in advancing research across various scientific disciplines, ranging from materials science to molecular modeling, contributing to a deeper understanding of complex systems and phenomena. Researchers continue to explore and refine these methodologies, pushing the boundaries of computational physics and chemistry, and opening up new avenues for scientific exploration and innovation.

8 Conclusion and perspectives

RHEFs hold significant potential for developing materials capable of operating under extreme conditions. Over the past decade, researchers have been designing and investigating new RHEFs using magnetron sputtering as a deposition technique. This latter is commonly employed in the fabrication of films, offering the ability to achieve film thicknesses ranging from nanometers to micrometers on various substrate types. This deposition method is anticipated to expedite the development of RHEF applications, particularly those designed for extreme operating conditions. Utilizing this coating approach would significantly reduce the overall processing costs associated with using costly materials. Furthermore, magnetron sputtering can be used in reactive mode where a reactive gas can be introduced during deposition. This enables the deposition of ceramics like oxides, nitrides, or carbides offering then additional control over the film's properties. It is scalable and can be adapted for large-scale production in industry. This makes it a preferred choice for manufacturing applications. However, despite its potential, studies investigating RHEFs using this technique remain very limited. Further efforts are necessary to enhance our understanding of the intricate relationship between the microstructure, mechanical, functional properties, and physicochemical attributes of these layers.

Regarding the structure, RHEFs can be divided into three different types: bcc, fcc, and amorphous or nanocrystalline structure. A phase transformation occurred under the effect two majors' parameters: the addition of element and the temperature. The formation of nitrides, e.g., the addition of nitrogen leads to the phase change from amorphous to bcc or fcc. The addition of oxygen causes a phase transition from bcc to amorphous. However, by adding Zr with low content, the structure of RHEF changes from crystal to amorphous with a crystal-amorphous dual-phase was formed with high Zr content. Even, the increasing of the temperature showed a phase transformation from amorphous to bcc. The phase transformation of these different RHEFs could be one of the reasons for their improved performances. Moreover, the results have demonstrated that the use of transmission

microscopy is a crucial technique that allows for an in-depth understanding of the structure of RHEF where the limitation of X-ray diffraction is evident.

In the case of the oxidation phenomenon of RHEFs, the addition of elements such as Si, Al, or Cr has been reported to improve their oxidation resistance. Protective layers, namely SiO_3 , Al_2O_3 , or Cr_2O_3 were formed acting as barriers to oxygen diffusion. It was demonstrated that at low temperatures, the growth of oxides is slower due to sluggish diffusion. However, with increasing the temperature atomic diffusion accelerates leading to more oxidation processes. The formation of nitrides has shown potential in countering the oxidation phenomenon compared to the free-nitrogen RHEFs. While, these results suggest the possibility of improving the oxidation resistance of RHEFs, studies in this regard are very limited. Further investigations are needed to gain a deep understanding of this phenomenon.

Enhanced mechanical properties, particularly hardness, have been achieved through several factors: the incorporation of metallic elements, nitrogen addition, temperature variations, and substrate bias. The ratio of metal to nitrogen an control phase formation. The formation of the fcc phase was demonstrated to increase the hardness. In the case of CrHfMoTaW nitrides, hardness decreases with increasing temperature. The addition of metallic elements also affects hardness. For example, adding of W and Mo to TiZrHfNbTa leads to a higher strengthening effect due to the formation small Mo or W-rich nanocrystallites. Other deposition parameters in the magnetron sputtering process also affect the mechanical properties of RHEFs. The bias has been shown to improve the film hardness with highest value obtained for RHEFs prepared by magnetron sputtering reaching about 30 GPa. The change in microstructure, whether dense or porous films is the main reason for the variation in hardness. Conversely, the investigation of tribological performances of RHEFs is very limited, thus further studies are necessary to better understand this phenomenon.

RHEFs have demonstrated promising functional attributes, particularly in term of corrosion resistance. Studies of RHEFs have shown their to outperform commonly used stainless steel in combating corrosion. Moreover, the incorporation of elements such as Al and Ag in RHEFs has revealed their highest protective attributed to the lower porosity of the film.

RHEFs have demonstrated promising functional attributes, particularly in terms of corrosion resistance. Studies have shown their potential to outperform commonly used stainless steel in combating corrosion. Additionally, the incorporation of elements such as Al and Ag in RHEFs has revealed their highest protective efficiency, attributed to the lower porosity of the film. Utilizing thermodynamic criteria to predict phases offers an approach to discern the possible combinations of multiple metallic elements. Predictions have successfully identified solid solutions and intermetallic compounds in various HEAs. However, this

approach is still relatively limited when applied to films, especially those produced through magnetron sputtering. Several unexplored avenues remain in understanding the correlation between prediction criteria and the diverse parameters involved in film deposition. Further investigations are required to address questions about the applicability of these criteria to ceramic deposition, including variations in gas flows (N_2 , O_2 , and CH_4/C_2H_6).

In recent years, computer technology has witnessed rapid growth in material calculation and simulation studies, enabling the resolution of errors inherent in conventional experimental methods. Presently, artificial intelligence is garnering increasing research focus for materials study and prediction, presenting significant potential for applications in fields like HEAs/HEFs. Leveraging a combination of thermodynamic databases and DFT calculations offers unparalleled advantages for data mining and guiding experimental design. Compared to classical computers, quantum computers are expected to provide exponential speedup and enhanced efficiency due to qubit entanglement. Quantum computers can utilize algorithms such as Shor's and Grover's to achieve this.

In general, due to their distinctive features and inherent attributes, HEFs and specifically RHEFs are expected to pave the way for numerous potential applications in the coming years. These applications are versatile and span various domains.

Owing to their heightened capacity to withstand wear and endure intense friction, high-entropy films present a distinctive potential application in the field of wear resistance. These alloys can be utilized to safeguard cutting tools, bearing materials, and mechanical components due to their unique properties. Their exceptional characteristics render them suitable for coating surfaces that require critical sensitivity.

Furthermore, the consistent composition of HEFs, combined with their inherent stability, makes them ideal candidates for applications in the realm of corrosion resistance. Consequently, these alloys can be employed to safeguard coatings in highly challenging technological environments, such as underwater domains or aerospace settings.

In the context of optoelectronics and electronics, HEFs' exceptional capability to modify their constituents and finely adjust their characteristics places them as a favorable option for fabricating high-performance sensors, photodetectors, and electronic devices.

Let us zero in catalytic applications—an exciting topic. The unique compositions of HEFs, coupled with their extensive surface area, are poised to achieve remarkable advancements in environmental restoration and chemical processing, to name just a few examples of potential applications.

Delving into energy conversion and storage—an exciting frontier—particularly in car battery technology, fuel cells,

and supercapacitors. The ability to create HEFs with specific combinations of elements establishes the route for significant advancements in addressing the growing energy crisis.

When exploring the field of biomedical innovation, HEFs demonstrate a remarkable propensity for adaptation, attributed to their surface interactions and inherent characteristics. These applications could cover a broad spectrum of technologies, ranging from biocompatible coatings to drug delivery systems and implant materials.

Last but not least, the downscaled dimensions of HEFs offer intriguing possibilities for engineering applications. Thanks to their distinguished properties, HEFs can be seamlessly integrated into nanoscale devices. Notable areas of promise include nanoelectromechanical systems (NEMS) and nanoscale sensors for various domains.

Through these avenues, the future of HEFs holds immense promise for enhancing various industries, driving innovation, and pushing the boundaries of what's possible in material science and technology.

Acknowledgements The authors thank the Université de Technologie de Troyes (UTT), le Conseil départemental de l'Aube (CD10), Groupement d'intérêt public Haute Marne (GIP52), and the University of Cadi Ayyad.

Author contribution M.E. and D.S.: conceptualization, writing—original draft preparation, review and editing; F.S.: review and editing. All authors have read and agreed to the published version of the manuscript.

Declarations

Conflict of interest The authors declare no competing interests.

Open Access This article is licensed under a Creative Commons Attribution 4.0 International License, which permits use, sharing, adaptation, distribution and reproduction in any medium or format, as long as you give appropriate credit to the original author(s) and the source, provide a link to the Creative Commons licence, and indicate if changes were made. The images or other third party material in this article are included in the article's Creative Commons licence, unless indicated otherwise in a credit line to the material. If material is not included in the article's Creative Commons licence and your intended use is not permitted by statutory regulation or exceeds the permitted use, you will need to obtain permission directly from the copyright holder. To view a copy of this licence, visit <http://creativecommons.org/licenses/by/4.0/>.

References

1. J.W. Yeh, S.K. Chen, S.J. Lin, J.Y. Gan, T.S. Chin, T.T. Shun et al., Nanostructured high-entropy alloys with multiple principal elements: novel alloy design concepts and outcomes. *Adv. Eng. Mater.* **6**(5), 299–303 (2004). <https://doi.org/10.1002/adem.200300567>
2. B. Cantor, I. Chang, P. Knight, A. Vincent, Microstructural development in equiatomic multicomponent alloys. *Mater. Sci. Eng. A* **375**, 213–218 (2004). <https://doi.org/10.1016/j.msea.2003.10.257>

3. M.C. Gao, J.-W. Yeh, P.K. Liaw, Y. Zhang, High-entropy alloys: fundamentals and applications, eds. (Springer International Publishing, Cham, 2016), pp. 51
4. O. Senkov, J. Miller, D. Miracle, C. Woodward, Accelerated exploration of multi-principal element alloys with solid solution phases. *Nat. Commun.* **6**(1), 6529 (2015). <https://doi.org/10.1038/ncomms7529>
5. D.B. Miracle, O.N. Senkov, A critical review of high entropy alloys and related concepts. *Acta Mater.* **122**, 448–511 (2017). <https://doi.org/10.1016/j.actamat.2016.08.081>
6. K. Cui, Y. Zhang, High-entropy alloy films. *Coatings* **13**(3), 635 (2023). <https://doi.org/10.1080/21663831.2018.1434248>
7. M. El Garah, P. Briois, F. Sanchette, Recent progress on high-entropy films deposited by magnetron sputtering. *Crystals* **12**(3), 335 (2022). <https://doi.org/10.3390/cryst12030335>
8. N.I. Muhammad Nadzri, D.S.C. Halin, M.M. Al Bakri Abdullah, S. Joseph, M.A.A. Mohd Salleh, P. Vitureanu, et al., High-entropy alloy for thin film application: a review. *Coatings* **12**(12), 1842 (2022). <https://doi.org/10.3390/coatings12121842>
9. Y. Liu, D. Xiang, K. Wang, T. Yu, Corrosion of laser cladding high-entropy alloy coatings: a review. *Coatings* **12**(11), 1669 (2022). <https://doi.org/10.3390/coatings12111669>
10. B. Xing, Q. Ding, B. Jin, X. Zuo, N. Zhang, S. Yin, Corrosion resistance and passivation behavior of CoCrFeNi-TiAl high-entropy alloy coatings in acidic solutions. *J. Therm. Spray Technol.* **31**(5), 1673–1682 (2022). <https://doi.org/10.1007/s11666-022-01380-6>
11. W. Li, P. Liu, P.K. Liaw, Microstructures and properties of high-entropy alloy films and coatings: a review. *Mater. Res. Lett.* **6**(4), 199–229 (2018). <https://doi.org/10.1080/21663831.2018.1434248>
12. P. Zhang, Z. Li, H. Liu, Y. Zhang, H. Li, C. Shi et al., Recent progress on the microstructure and properties of high entropy alloy coatings prepared by laser processing technology: a review. *J. Manuf. Process.* **76**, 397–411 (2022). <https://doi.org/10.1016/j.jmapro.2022.02.006>
13. C. Oses, C. Toher, S. Curtarolo, High-entropy ceramics. *Nat. Rev. Mater.* **5**(4), 295–309 (2020). <https://doi.org/10.1038/s41578-019-0170-8>
14. D. Luo, Q. Zhou, Z. Huang, Y. Li, Y. Liu, Q. Li et al., Tribological behavior of high entropy alloy coatings: a review. *Coatings* **12**(10), 1428 (2022). <https://doi.org/10.3390/coatings12101428>
15. W. Li, D. Xie, D. Li, Y. Zhang, Y. Gao, P.K. Liaw, Mechanical behavior of high-entropy alloys. *Prog. Mater. Sci.* **118**, 100777 (2021). <https://doi.org/10.1016/j.pmatsci.2021.100777>
16. X. Wang, W. Guo, Y. Fu, High-entropy alloys: emerging materials for advanced functional applications. *J. Mater. Chem. A.* **9**(2), 663–701 (2021). <https://doi.org/10.1039/D0TA09601F>
17. S. Praveen, H.S. Kim, High-entropy alloys: potential candidates for high-temperature applications—an overview. *Adv. Eng. Mater.* **20**(1), 1700645 (2018). <https://doi.org/10.1002/adem.201700645>
18. A. Sharma, High entropy alloy coatings and technology. *Coatings* **11**(4), 372 (2021). <https://doi.org/10.3390/coatings11040372>
19. E. Fermi, Sopra lo spostamento per Pressione delle Righe Elevate delle Serie Spettrali. *Il Nuovo Cim.* (1924–1942) **11**(3), 157–66 (1934). <https://doi.org/10.1007/BF02959829>
20. H. Axon, W. Hume-Rothery, The lattice spacings of solid solutions of different elements in aluminium. *Proc. R. Soc. Lond. Ser. A Math. Phys. Sci.* **193**(1032), 1–24 (1948). <https://doi.org/10.1098/rspa.1948.0030>
21. A. Inoue, Stabilization of metallic supercooled liquid and bulk amorphous alloys. *Acta Mater.* **48**(1), 279–306 (2000). [https://doi.org/10.1016/S1359-6454\(99\)00300-6](https://doi.org/10.1016/S1359-6454(99)00300-6)
22. Y. Zhang, Y.J. Zhou, J.P. Lin, G.L. Chen, P.K. Liaw, Solid-solution phase formation rules for multi-component alloys. *Adv. Eng. Mater.* **10**(6), 534–538 (2008). <https://doi.org/10.1002/adem.200700240>
23. E. Schrödinger, An undulatory theory of the mechanics of atoms and molecules. *Phys. Rev.* **28**(6), 1049 (1926). <https://doi.org/10.1103/PhysRev.28.1049>
24. M. Born, K. Huang, M. Lax, Dynamical theory of crystal lattices. *Am. J. Phys.* **23**(7), 474 (1955). <https://doi.org/10.1107/S0365110X56002370>
25. F. Otto, Y. Yang, H. Bei, E.P. George, Relative effects of enthalpy and entropy on the phase stability of equiatomic high-entropy alloys. *Acta Mater.* **61**(7), 2628–2638 (2013). <https://doi.org/10.1016/j.actamat.2013.01.042>
26. D. Soubane, M. El Garah, M. Bouhassoune, A. Tirbiyine, A. Ramzi, S. Laasri, Hidden information, energy dispersion and disorder: does entropy really measure disorder? *World J. Condens. Matter Phys.* **8**(4), 197–202 (2018). <https://doi.org/10.4236/wjcmp.2018.84014>
27. Q. Xing, J. Ma, C. Wang, Y. Zhang, High-throughput screening solar-thermal conversion films in a pseudobinary (Cr, Fe, V)–(Ta, W) system. *ACS Comb. Sci.* **20**(11), 602–610 (2018). <https://doi.org/10.1021/acscombsci.8b00055>
28. D.B. Miracle, J.D. Miller, O.N. Senkov, C. Woodward, M.D. Uchic, J. Tiley, Exploration and development of high entropy alloys for structural applications. *Entropy* **16**(1), 494–525 (2014). <https://doi.org/10.3390/e16010494>
29. M.-H. Tsai, J.-W. Yeh, High-entropy alloys: a critical review. *Mater. Res. Lett.* **2**(3), 107–123 (2014). <https://doi.org/10.1080/21663831.2014.912690>
30. Y. Jien-Wei, Recent progress in high entropy alloys. *Ann. Chim. Sci. Mat.* **31**(6), 633–648 (2006)
31. B. Murty, J.W. Yeh i S. Ranganathan, High-entropy alloys. (Elsevier, Amsterdam, 2014), p. 13–35
32. D.R. Gaskell, D.E. Laughlin, Introduction to the thermodynamics of materials. (6th edn. (CRC Press, Boca Raton 2017)
33. R.A. Swalin, Thermodynamics of solids. *J. Electrochem. Soc.* **109**(12), 308C (1972)
34. J.-W. Yeh, Alloy design strategies and future trends in high-entropy alloys. *Jom* **65**, 1759–1771 (2013). <https://doi.org/10.1007/s11837-013-0761-6>
35. W. Hume-Rothery, The structure of metals and alloys. *Indian J. Phys.* **11**, 74 (1969). <https://doi.org/10.1038/138007a0>
36. O. Senkov, D. Miracle, A new thermodynamic parameter to predict formation of solid solution or intermetallic phases in high entropy alloys. *J. Alloy. Compd.* **658**, 603–607 (2016)
37. W. Cheng, L. Ji, L. Zhang, H. Wang, W. Sun, Refractory high-entropy alloys fabricated using laser technologies: a concrete review. *J. Market. Res.* (2023). <https://doi.org/10.1016/j.jmrt.2023.05.037>
38. B. Chen, L. Zhuo, Latest progress on refractory high entropy alloys: composition, fabrication, post processing, performance, simulation and prospect. *Int. J. Refract. Met. Hard Mater.*, 105993 (2022). <https://doi.org/10.1016/j.ijrmhm.2022.105993>
39. A. Billard, F. Perry, Pulvérisation cathodique magnétron, Techniques de l'ingénieur. *Matér. Métalliques.* **8733**, 2005 (1762)
40. D.M. Mattox, Physical vapor deposition (PVD) processes. *Met. Finish.* **100**, 394–408 (2002). [https://doi.org/10.1016/S0026-0576\(02\)82043-8](https://doi.org/10.1016/S0026-0576(02)82043-8)
41. C. Manasterski, La pulvérisation cathodique industrielle. (PPUR presses polytechniques, 2005)
42. N.S. Peighambaroust, A.A. Alamdari, U. Unal, A. Motallebzadeh, In vitro biocompatibility evaluation of Ti1. 5ZrTa0. 5Nb0. 5Hf0. 5 refractory high-entropy alloy film for orthopedic implants: microstructural, mechanical properties and corrosion behavior. *J. Alloys Compd.* **883**, 160786 (2021)

43. A.A. Alamdari, U. Unal, A. Motallebzadeh, Investigation of microstructure, mechanical properties, and biocorrosion behavior of Ti1.5ZrTa0.5Nb0.5W0.5 refractory high-entropy alloy film doped with Ag nanoparticles. *Surf. Interfaces* **28**, 101617 (2022). <https://doi.org/10.1016/j.vacuum.2022.111286>
44. H. Kim, S. Nam, A. Roh, M. Son, M.-H. Ham, J.-H. Kim et al., Mechanical and electrical properties of NbMoTaW refractory high-entropy alloy thin films. *Int. J. Refract. Met. Hard Mater.* **80**, 286–291 (2019). <https://doi.org/10.1016/j.ijrmhm.2019.02.005>
45. B.-S. Lou, C.-J. Wang, Y.-Y. Chen, S.-B. Hung, Y.-C. Lin, J.-W. Lee, Phase, mechanical property and corrosion resistance evaluation of W-Nb-Ta-Ti and W-Nb-Ta-Ti-N medium entropy alloy thin films. *Surf. Coat. Technol.* **442**, 128339 (2022)
46. F. Cemin, M.J. Jimenez, L.M. Leidens, C.A. Figueroa, F. Alvarez, A thermodynamic study on phase formation and thermal stability of AlSiTaTiZr high-entropy alloy thin films. *J. Alloy. Compd.* **838**, 155580 (2020)
47. K. Alam, G. Jeong, W. Jang, H. Cho, Enhanced mechanical properties and in vitro biocompatibility of TiMOVWCr high-entropy alloy synthesized by magnetron sputtering. *Appl. Surf. Sci.* **639**, 158222 (2023). <https://doi.org/10.1016/j.apsusc.2023.158222>
48. B. Wu, Y. Wang, Y. Yu, F. Jiang, H. Sun, F. Jing et al., Modulate the deposition rate through changing the combination of frequency and pulse width at constant duty cycle. *Surf. Coat. Technol.* **281**, 27–34 (2015)
49. Y. Li, C. Wang, D. Ma, X. Zeng, M. Liu, X. Jiang et al., Nano dual-phase CuNiTiNbCr high entropy alloy films produced by high-power pulsed magnetron sputtering. *Surf. Coat. Technol.* **420**, 127325 (2021). <https://doi.org/10.1016/j.surfcoat.2021.127325>
50. X. Yin, H. Wang, J. Xiao, Y. Sun, K. Zhao, J. Wu et al., A high-entropy alloy nitride protective coating for fuel cladding in high temperature lead-bismuth eutectic alloy. *J. Nucl. Mater.* **568**, 153888 (2022). <https://doi.org/10.1016/j.jnucmat.2022.153888>
51. U. Helmersson, M. Lattemann, J. Bohlmark, A.P. Ehiassarian, J.T. Gudmundsson, Ionized physical vapor deposition (IPVD): a review of technology and applications. *Thin Solid Films* **513**(1–2), 1–24 (2006). <https://doi.org/10.1016/j.tsf.2006.03.033>
52. M. Michiels, S. Konstantinidis, R. Snyders, La Pulvérisation Cathodique Magnétron en Régime D'impulsions de Haute Puissance (Hipims). In : *Techniques de l'ingénieur*, 2013
53. S.-Y. Tsai, Y.-A. Chen, J.-D. You, J.P. Chu, P. Yiu, Micro-scale tribological study of a Ni-Cr-Fe-Ti-Al-V high entropy alloy thin film by magnetron co-sputtering of Inconel-718 and Ti-6Al-4V. *Surf. Coat. Technol.* **464**, 129481 (2023). <https://doi.org/10.1016/j.surfcoat.2023.129481>
54. Z. Yang, N. Qiu, H. Yang, Q. Chen, Y. Wang, Irradiation tolerance enhanced by coherent interfaces of FCC/BCC HEA multilayers. *Surf. Coat. Technol.* **457**, 129338 (2023). <https://doi.org/10.1016/j.surfcoat.2023.129338>
55. S.S. Oladijo, F.M. Mwema, T.C. Jen, K. Ronoh, D. Sobola, E.T. Akinlabi, Nanoscale surface dynamics of RF-magnetron sputtered CrCoCuFeNi high entropy alloy thin films. *Mater. Today Commun.* **33**, 104523 (2022). <https://doi.org/10.1016/j.mtcomm.2022.104523>
56. N.G. Kipkirui, T.-T. Lin, R.S. Kiplangat, J.-W. Lee, S.-H. Chen, HiPIMS and RF magnetron sputtered Al0.5CoCrFeNi2Ti0.5 HEA thin-film coatings: synthesis and characterization. *Surf. Coat. Technol.* **449**, 128988 (2022). <https://doi.org/10.1016/j.surfcoat.2022.128988>
57. X. Zhang, X. Zeng, Y. Liu, J. Liu, A. Pogrebnyak, V. Pelenovich et al., Effects of RF magnetron sputtering power on the structure and nanohardness of high-entropy alloys (TiVCrNbSiTaBY)N hard coatings. *Ceram. Int.* **49**(20), 33418–33424 (2023). <https://doi.org/10.1016/j.ceramint.2023.08.020>
58. W. Xiong, A.X. Guo, S. Zhan, C.-T. Liu, S.C. Cao, Refractory high-entropy alloys: a focused review of preparation methods and properties. *J. Mater. Sci. Technol.* **142**, 196–215 (2023)
59. A. Xia, R. Dedoncker, O. Glushko, M.J. Cordill, D. Depla, R. Franz, Influence of the nitrogen content on the structure and properties of MoNbTaVW high entropy alloy thin films. *J. Alloy. Compd.* **850**, 156740 (2021). <https://doi.org/10.1016/j.jallcom.2020.156740>
60. A. Xia, A. Togni, S. Hirn, G. Bolelli, L. Lusvarghi, R. Franz, Angular-dependent deposition of MoNbTaVW HEA thin films by three different physical vapor deposition methods. *Surf. Coat. Technol.* **385**, 125356 (2020). <https://doi.org/10.1016/j.surfcoat.2020.125356>
61. S. Fritze, C.M. Koller, L. von Fieandt, P. Malinovskis, K. Johansson, E. Lewin et al., Influence of deposition temperature on the phase evolution of HfNbTiVZr high-entropy thin films. *Materials* **12**(4), 587 (2019). <https://doi.org/10.3390/ma12040587>
62. L. Bi, X. Li, Z. Li, Y. Hu, J. Zhang, Q. Wang et al., Performance and local structure evolution of NbMoTaWV entropy-stabilized oxide thin films with variable oxygen content. *Surf. Coat. Technol.* **402**, 126326 (2020). <https://doi.org/10.1016/j.surfcoat.2020.126326>
63. X. Feng, S. Fan, F. Meng, J.U. Surjadi, K. Cao, W. Liao et al., Effect of Zr addition on microstructure and mechanical properties of CoCrFeNiZr x high-entropy alloy thin films. *Appl. Nanosci.* **11**, 771–776 (2021)
64. W. Liao, S. Lan, L. Gao, H. Zhang, S. Xu, J. Song et al., Nanocrystalline high-entropy alloy (CoCrFeNiAl0.3) thin-film coating by magnetron sputtering. *Thin Solid Films* **638**, 383–8 (2017)
65. M. El Garah, L. Patout, A. Bouissil, A. Charai, F. Sanchette, The effect of yttrium addition on microstructure and mechanical properties of refractory TiTaZrHfW high-entropy films. *Coatings* **13**(8), 1380 (2023). <https://doi.org/10.3390/coatings13081380>
66. D.E. Touaibia, S. Achache, A. Bouissil, J. Ghanbaja, S. Migot, M.A.P. Yazdi et al., Oxidation resistance and mechanical properties of AlTiZrHfTa(-N) high entropy films deposited by reactive magnetron sputtering. *J. Alloy. Compd.* **969**, 172397 (2023). <https://doi.org/10.1016/j.jallcom.2023.172397>
67. T. Stasiak, P. Souček, V. Buršíková, N. Koutná, Z. Czigány, K. Balázsi et al., Synthesis and characterization of the ceramic refractory metal high entropy nitride thin film from Cr-Hf-Mo-Ta-W system. *Surf. Coat. Technol.* **449**, 128987 (2022). <https://doi.org/10.1016/j.surfcoat.2022.128987>
68. C. Cheng, X. Zhang, M.J. Haché, Y. Zou, Phase transition and nanomechanical properties of refractory high-entropy alloy thin films: effects of co-sputtering Mo and W on a TiZrHfNbTa system. *Nanoscale* **14**(20), 7561–7568 (2022). <https://doi.org/10.1039/D2NR01635D>
69. C. Zhan, D. Huang, X. Hu, K. Xu, M. Lou, L. Chen et al., Mechanical property enhancement of NbTiZr refractory medium-entropy alloys due to Si-induced crystalline-to-amorphous transitions. *Surf. Coat. Technol.* **433**, 128144 (2022). <https://doi.org/10.1016/j.surfcoat.2022.128144>
70. Y. Zhang, X.-H. Yan, W.-B. Liao, K. Zhao, Effects of nitrogen content on the structure and mechanical properties of (Al0.5CrFeNiTi0.25)Nx high-entropy films by reactive sputtering. *Entropy* **20**(9), 624 (2018)
71. W.-B. Liao, H. Zhang, Z.-Y. Liu, P.-F. Li, J.-J. Huang, C.-Y. Yu et al., High strength and deformation mechanisms of Al0.3CoCrFeNi high-entropy alloy thin films fabricated by magnetron sputtering. *Entropy* **21**(2), 146 (2019)
72. F. Cemin, S.R. de Mello, C.A. Figueroa, F. Alvarez, Influence of substrate bias and temperature on the crystallization of metallic

- NbTaTiVZr high-entropy alloy thin films. *Surf. Coat. Technol.* **421**, 127357 (2021). <https://doi.org/10.1016/j.surfcoat.2021.127357>
73. J. Wang, X. Liu, Y. Zhang, W. Cai, L. Wang, L. Tang, Effect of substrate bias on the microstructure and mechanical and tribological properties of ZrNbTiMo refractory high entropy alloy film. *Surf. Coat. Technol.* **455**, 129214 (2023). <https://doi.org/10.1016/j.surfcoat.2022.129214>
 74. X. Liu, W. Cai, Y. Zhang, L. Wang, J. Wang, Tuning microstructure and mechanical and wear resistance of ZrNbTiMo refractory high-entropy alloy films via sputtering power. *Front. Mater.* **10**, 1145631 (2023). <https://doi.org/10.3389/fmats.2023.1145631>
 75. Q. Xing, A.C. Feltrin, F. Akhtar, High-temperature wear properties of CrFeHfMnTiTaV septenary complex concentrated alloy film produced by magnetron sputtering. *Wear* **510**, 204497 (2022). <https://doi.org/10.1016/j.wear.2022.204497>
 76. W.-B. Liao, C.-H. Xu, T.-L. Wang, C.-S. Feng, M.A. Khan, G. Yasin, Oxidation influences on the microstructure and mechanical properties of W-Nb-Mo-Ta-V-O refractory high-entropy alloy films. *Vacuum* **207**, 111586 (2023). <https://doi.org/10.1016/j.vacuum.2022.111586>
 77. A. Bouissil, S. Achache, D.E. Touaibia, B. Panicaud, M.A.P. Yazdi, F. Sanchette et al., Properties of a new TiTaZrHfW (N) refractory high entropy film deposited by reactive DC pulsed magnetron sputtering. *Surf. Coat. Technol.* **462**, 129503 (2023). <https://doi.org/10.1016/j.surfcoat.2023.129503>
 78. S.K. Bachani, C.-J. Wang, B.-S. Lou, L.-C. Chang, J.-W. Lee, Microstructural characterization, mechanical property and corrosion behavior of VNbMoTaWAl refractory high entropy alloy coatings: effect of Al content. *Surf. Coat. Technol.* **403**, 126351 (2020). <https://doi.org/10.1016/j.surfcoat.2020.126351>
 79. A.A. Alamdari, M. Hashemkhani, S. Hendessi, P.T. Guner, H.Y. Acar, I.H. Kavakli et al., In vitro antibacterial and cytotoxicity assessment of magnetron sputtered Ti1.5ZrTa0.5Nb0.5W0.5 refractory high-entropy alloy doped with Ag nanoparticles. *Vacuum* **203**, 111286 (2022). <https://doi.org/10.1016/j.vacuum.2022.111286>
 80. C.-S. Feng, T.-W. Lu, T.-L. Wang, M.-Z. Lin, J. Hou, W. Lu et al., A novel high-entropy amorphous thin film with high electrical resistivity and outstanding corrosion resistance. *Acta Metall. Sin. (Engl. Lett.)* **34**(11), 1537–1545 (2021)
 81. O. El-Atwani, N. Li, M. Li, A. Devaraj, J. Baldwin, M.M. Schneider et al., Outstanding radiation resistance of tungsten-based high-entropy alloys. *Sci. Adv.* **5**(3), eaav2002 (2019). <https://doi.org/10.1126/sciadv.aav2002>
 82. J. Wang, R. Shu, A. Elskukova, S.G. Rao, J. Chai, Y. Zhu et al., Structural stability under Xe-ion irradiation of TiZrNbTaV-based high-entropy alloy and nitride films. *Surf. Coat. Technol.* **454**, 129198 (2023). <https://doi.org/10.1016/j.surfcoat.2022.129198>
 83. G. Pu, S. Sun, S. Wang, L. Gan, S. Chen, Z. Ye et al., A comparative study of irradiation response in amorphous TaTiWVCr refractory high entropy alloy with the counterpart of tungsten films. *Intermetallics* **156**, 107850 (2023). <https://doi.org/10.1016/j.intermet.2023.107850>
 84. Y.-Y. Chen, S.-B. Hung, C.-J. Wang, W.-C. Wei, J.-W. Lee, High temperature electrical properties and oxidation resistance of V-Nb-Mo-Ta-W high entropy alloy thin films. *Surf. Coat. Technol.* **375**, 854–863 (2019). <https://doi.org/10.1016/j.surfcoat.2019.07.080>
 85. L. Gao, J. Song, Z. Jiao, W. Liao, J. Luan, J.U. Surjadi et al., High-entropy alloy (HEA)-coated nanolattice structures and their mechanical properties. *Adv. Eng. Mater.* **20**(1), 1700625 (2018)
 86. C. Feng, X. Feng, Z. Guan, H. Song, T. Wang, W. Liao et al., Nanocrystalline (AlTiVCr)N multi-component nitride thin films with superior mechanical performance. *Nanomaterials* **12**(15), 2722 (2022)
 87. P. Hohenberg, W. Kohn, Inhomogeneous electron gas. *Phys. Rev.* **136**(3B), B864 (1964). <https://doi.org/10.1103/PhysRev.136.B864>
 88. W. Kohn, L.J. Sham, Self-consistent equations including exchange and correlation effects. *Phys. Rev.* **140**(4A), A1133 (1965). <https://doi.org/10.1103/PhysRev.140.A1133>
 89. L.H. Thomas, *The calculation of atomic fields* (Cambridge University Press, Mathematical proceedings of the Cambridge philosophical society, 1927), pp.542–548
 90. J.P. Perdew, K. Schmidt, Jacob's ladder of density functional approximations for the exchange-correlation energy. *AIP Conf. Proc.* **577**, 1–20 (2001). <https://doi.org/10.1063/1.1390175>
 91. P. Ganesh, M. Widom, Ab initio simulations of geometrical frustration in supercooled liquid Fe and Fe-based metallic glass. *Phys. Rev. B* **77**(1), 014205 (2008). <https://doi.org/10.1103/PhysRevB.77.014205>
 92. W.P. Huhn, M. Widom, A.M. Cheung, G.J. Shiflet, S.J. Poon, J. Lewandowski, First-principles calculation of elastic moduli of early-late transition metal alloys. *Phys. Rev. B* **89**(10), 104103 (2014). <https://doi.org/10.1103/PhysRevB.89.104103>
 93. M. Mihalkovič, M. Widom, Ab initio calculations of cohesive energies of Fe-based glass-forming alloys. *Phys. Rev. B* **70**(14), 144107 (2004). <https://doi.org/10.1103/PhysRevB.70.144107>
 94. M. Widom, W.P. Huhn, S. Maiti, W. Steurer, Hybrid Monte Carlo/molecular dynamics simulation of a refractory metal high entropy alloy. *Metall. Mater. Trans. A* **45**, 196–200 (2014). <https://doi.org/10.1007/s11661-013-2000-8>
 95. A. Inoue, Stabilization and high strain-rate superplasticity of metallic supercooled liquid. *Mater. Sci. Eng. A* **267**(2), 171–183 (1999). [https://doi.org/10.1016/S0921-5093\(99\)00089-1](https://doi.org/10.1016/S0921-5093(99)00089-1)
 96. M.C. Tropicovsky, J.R. Morris, P.R. Kent, A.R. Lupini, G.M. Stocks, Criteria for predicting the formation of single-phase high-entropy alloys. *Phys. Rev. X* **5**(1), 011041 (2015). <https://doi.org/10.1103/PhysRevX.5.011041>
 97. H. Hellmann, A new approximation method in the problem of many electrons. *J. Chem. Phys.* **3**(1), 61 (1935). <https://doi.org/10.1063/1.1749559>
 98. G. Kresse, J. Furthmüller, Efficient iterative schemes for ab initio total-energy calculations using a plane-wave basis set. *Phys. Rev. B* **54**(16), 11169 (1996). <https://doi.org/10.1103/PhysRevB.54.11169>
 99. G. Kresse, J. Hafner, Ab initio molecular dynamics for liquid metals. *Phys. Rev. B* **47**(1), 558 (1993). <https://doi.org/10.1103/PhysRevB.47.558>
 100. N.W. Ashcroft, N.D. Mermin, *Solid state physics* (Holt, Rinehart and Winston New York, New York, 1976)
 101. M. Born, K. Huang, Dynamical theory of crystal lattices. *Am. J. Phys.* **1954**, 474 (1955)
 102. C. Kittel, *Introduction to solid state physics*. John Wiley & Sons, 8th edn, 2005
 103. G. Makov, M.C. Payne, Periodic boundary conditions in ab initio calculations. *Phys. Rev. B* **51**(7), 4014 (1995). <https://doi.org/10.1103/PhysRevB.51.4014>
 104. P. Giannozzi, S. Baroni, N. Bonini, M. Calandra, R. Car, C. Cavazzoni et al., QUANTUM ESPRESSO: a modular and open-source software project for quantum simulations of materials. *J. Phys.: Condens. Matter* **21**(39), 395502 (2009). <https://doi.org/10.1088/0953-8984/21/39/395502>
 105. W. Hehre, W. Lathan, R. Ditchfield, M. Newton, J. Pople, *Gaussian 70* (Chemistry Department, Indiana University, Bloomington, Indiana, Quantum Chemistry Program Exchange, 1970)
 106. D. Young, Appendix AA 2.4 Gaussian. *Computational Chemistry*. (Wiley-Interscience, 2001), p. 336
 107. F. Neese, The ORCA program system. *Wiley Interdisc. Rev.: Comput. Mol. Sci.* **2**(1), 73–78 (2012). <https://doi.org/10.1002/wcms.81>

- 108 F. Neese, Software update: the ORCA program system, version 4.0. *Wiley Interdisc. Rev.: Comput. Mol. Sci.* **8**(1), 1327 (2018). <https://doi.org/10.1002/wcms.1327>
109. F. Neese, F. Wennmohs, U. Becker, C. Riplinger, The ORCA quantum chemistry program package. *J. Chem. Phys.* **152**(22) (2020). <https://doi.org/10.1063/5.0004608>
- 110 F. Neese, Software update: the ORCA program system—version 5.0. *Wiley Interdisc. Rev.: Comput. Mol. Sci.* **12**(5), 1606 (2022). <https://doi.org/10.1002/wcms.1606>